Adaptive Gap-Filling of Multi-Spectral Images at Coarse and Fine Spatial Resolution

Afsharipour, Seyedkarim; Jia, Li; Menenti, Massimo; Malamiri, Hamid Reza Ghafarian

DOI
10.1109/JSTARS.2025.3551360

Publication date
2025

Document Version
Final published version

Published in
IEEE Journal of Selected Topics in Applied Earth Observations and Remote Sensing

JSTARS-2025-00370

Adaptive Gap-Filling of Multi-Spectral Images at Coarse and Fine Spatial Resolution

Seyedkarim Afsharipour, Li Jia, and Massimo Menenti, Hamid Reza Ghafarian Malamiri

***Abstract*— Optical fine and coarse spatial resolution multi-spectral images are essential for monitoring land surface processes but are often affected by gaps due to cloud contamination and other factors. Gap-filling methods are vital for overcoming these issues, yet existing approaches struggle to accurately reconstruct pixels impacted by undetected thin clouds and shadows, particularly in fine spatial resolution images. This study introduces a comprehensive gap-filling method that identifies and reconstructs invalid pixels in both fine and coarse spatial resolution images. The method combines different spatial and temporal gap-filling methods. The specific combination of methods is orchestrated to adapt to each image, mainly on the basis of the fractional abundance and spatial pattern of cloud cover. To evaluate the performance, experiments were conducted using MODIS (coarse-resolution) and Landsat/OLI (fine-resolution) images with artificial gaps (10%-90%) introduced at varying positions in cloud-free reference images. For coarse-resolution images, the blue band showed the lowest Root Mean Square Error (RMSE) of 0.004 to 0.03, while the NIR band had higher RMSE (0.01-0.05). The Structural Similarity Index Measure (SSIM) ranged from 0.96 to 0.73 as gap percentages increased. For fine-resolution images, random gaps were reconstructed most effectively, with RMSE values for the blue band between 0.005 and 0.01, and NIR errors ranging from 0.01 to 0.05. SSIM values ranged from 0.90 to 0.83 (blue) and 0.86 to 0.71 (NIR), confirming the method reliability for time-series analysis and data fusion applications.**

***Index Terms*— Gap-filling, Remote sensing, Invalid pixels, Coarse spatial resolution, Fine spatial resolution.**

This work was jointly funded by the project supported by the National Natural Science Foundation of China (NSFC) (Grant No. 42090014), the Open Research Program of the International Research Center of Big Data for Sustainable Development Goals (Grant No. CBAS2023OPR05), the Chinese Academy of Sciences President's International Fellowship Initiative (Grant No. 2025PVA0200, 2020VTA0001), the MOST High-Level Foreign Expert program (Grant No. G2022055010L), and the CAS-TWAS President's Fellowship Program. (Corresponding author: Li Jia).

Seyedkarim Afsharipour is with State Key Laboratory of Remote Sensing and Digital Earth, Aerospace Information Research Institute, Chinese Academy of Sciences. Beijing 100101, China and also with the University of Chinese Academy of Sciences, Beijing 100045, China (e-mail: seyedkarim@radi.ac.cn).

Li Jia is with State Key Laboratory of Remote Sensing and Digital Earth, Aerospace Information Research Institute, Chinese Academy of Sciences. Beijing 100101, China also with International Research Center of Big Data for Sustainable Development Goals, Beijing, China (e-mail: jiali@aircas.ac.cn).

Massimo Menenti is with State Key Laboratory of Remote Sensing and Digital Earth, Aerospace Information Research Institute, Chinese Academy of Sciences. Beijing 100101, China, Institute of Tibetan Plateau Research, Chinese Academy of Sciences, also with Faculty of Civil Engineering and Geosciences, Delft University of Technology, Delft, Netherlands (e-mail: m.menenti@radi.ac.cn).

Hamid Reza Ghafarian Malamiri is with Department of Geography, Yazd University, Yazd 8915818411, Iran (e-mail: hrghafarian@yazd.ac.ir).

I. INTRODUCTION

High spatial and temporal resolution multispectral remote sensing images acquired by space-borne sensors such as Landsat/OLI, Sentinel-2 sensor, and MODIS have transformed environmental monitoring by offering consistent, multi-temporal observations of the Earth surface [1]. In this study, these datasets are referred to as "fine-resolution images" (high spatial and low temporal resolution, e.g., Landsat/OLI) and "coarse-resolution images" (low spatial and high temporal resolution, e.g. MODIS) and are widely used across various applications due to their complementary characteristics. Applications include global change monitoring [2], [3], [4], [5], crop monitoring [6], [7], [8], [9], [10], [11], water resource management [8], [12], [13], [14], and others.

However, these datasets face persistent challenges, including contamination by clouds, shadows and aerosols, as well as sensor and algorithm malfunctions [15]. Such problems result in invalid and missing observations (gaps) in the spatial and temporal domains, significantly reducing the usability of both fine- and coarse-resolution images [16], [17]. Spatial gaps pose a greater challenge for analyses that rely on consistent and clear observations, such as Spatial and Temporal Fusion (STF) method [18], which aim to integrate fine- and coarse-resolution images [16], [19], [20]. Consequently, robust gap-filling techniques are required [21], to ensure and maximize the utilization of both fine- and coarse-resolution satellite data. To address this challenge, various gap-filling methods have been developed [21], [22], [23], [24], [25], [26].

Broadly speaking, gap-filling algorithms can be classified into three main categories: space-based, time-based and spatiotemporal (hybrid) methods [23]. The space-based methods rely solely on valid observations in the image containing spatial gaps to reconstruct the missing pixels. These methods assume that the missing and valid pixels within a single image (acquired on the same day) share similar statistical characteristics or texture information [27]. Notable examples of space-based methods include nearest neighbor interpolation [28], and the Kriging interpolation method [29]. While space-based methods are relatively easy to implement and computationally efficient, they typically perform well only for images with small gaps [23]. Furthermore, these methods tend to be less effective in regions with complex or heterogeneous

land cover, as they rely on the assumption of spatial homogeneity, which often does not hold in complex landscapes [24].

The time-based methods leverage valid observations from the same location at different times (usually from close temporal acquisitions) to fill missing pixels [30]. These approaches assume that the reflectance or spectral characteristics of a given pixel do not change significantly over short periods of time or have periodic behavior, making the temporal interpolation feasible for filling gaps. The time-based methods are commonly used for reconstructing values of gap pixels in images of coarse-resolution but high temporal frequency. For instance, the Harmonic ANalysis of Time Series (HANTS) model [31], [32], [33] uses temporal information to reconstruct and smooth image time series by fitting harmonic functions that capture periodic features such as seasonal vegetation cycles [34].

The spatiotemporal-based methods utilize both the spatial and temporal information to reconstruct missing pixels. These methods, often referred to as hybrid methods, leverage correlations across both spatial and temporal domains by integrating coarse-scale data with high temporal resolution and fine-scale data with high spatial resolution, thereby improving the gap-filling process. These approaches enable more robust reconstruction of missing data under varying conditions, improving the accuracy and reliability of the gap-filling process. Among the three types of gap-filling methods, spatiotemporal-based approaches provide a more reliable solution for reconstructing missing pixels [35], [36], [37]. This is supported by studies demonstrating that spatiotemporal methods leverage both spatial and temporal autocorrelation, leading to improved accuracy in pixel reconstruction [15], [35], [36], [37]. For example, one study highlighted that spatiotemporal techniques significantly improve data quality by utilizing information from both neighboring pixels and different time periods, resulting in superior performance in filling gaps in remote sensing data [38]. Furthermore, another investigation found that integrating spatiotemporal data with machine learning algorithms can lead high accuracy in reconstructing missing values, as demonstrated by validation against in situ measurements [35]. Nevertheless, there are still three primary challenges in gap-filling methodologies that must be addressed.

The first challenge arises from the inherently different characteristics of fine- and coarse-resolution imagery. While the gap-filling objective applies to both type of data, their distinct spatial and temporal characteristics require different gap-filling methodologies. Fine spatial resolution data, such as 30-meter resolution Landsat data, offer detailed spatial information critical for environmental monitoring, because the spatial patterns are much better delineated in high spatial resolution images [1], [39], [40]. Such data, however, have relatively low temporal resolution. In contrast, coarse spatial resolution images, such as MODIS with 250-1000meter resolution, provide high temporal resolution (e.g. daily observations) and are better suited for monitoring large-scale dynamic processes. The choice of distinct gap-filling methodologies for fine- and coarse-resolution images reflects the inherent trade-offs between their spatial and temporal resolutions. Despite these differences, existing methods often adopt a one-size-fits-all approach, which fails to leverage the unique characteristics of fine and coarse resolution imagery. Fine spatial resolution data, due to their sensitivity to spatial heterogeneity, require gap-filling methods that preserve spatial detail while avoiding artifacts that could distort fine-scale variability [41], [42]. This highlights the importance of tailored approaches to maintain data integrity in high-resolution applications. For instance, advanced interpolation or geostatistical methods, which are designed to reconstruct local spatial patterns, are often more suitable for fine-resolution data [43]. Conversely, coarse spatial data emphasize temporal continuity due to their frequent observations. Gap-filling approaches for gap-filling of coarse-resolution data must prioritize temporal consistency to ensure that the reconstructed values are consistent with the underlying temporal trends [44]. This often involves time-series-based techniques, such as harmonic analysis [45] or autoregressive models [46], which exploit the dense temporal information to predict missing values accurately. How-ever, these challenges differ significantly from those associated with fine-resolution data, where the accurate delineation of spatial patterns is paramount. The contrasting requirements underline the need for separate gap-filling methodologies that address the unique strengths and weaknesses of each type of data. The need for different methodologies is also underpinned by the intended applications of the gap-filled datasets. For instance, fine-resolution data support applications like as urban mapping [47], precision agriculture [48], and habitat monitoring [49], where spatial detail is paramount. Coarse-resolution data, however, facilitate large-scale studies such as phenological studies [50], [51], [52], climate monitoring, and biomass estimation [53], where temporal trends are paramount. In summary, the distinct spatial and temporal characteristics of fine- and coarse-resolution data require the use of separate gap-filling methods. For high-resolution images, spatial correlation is crucial for accurately reconstructing missing data, while for low-resolution images, leveraging temporal features is essential to fill the feature gaps. To the best of our knowledge, numerous gap-filling methods have been developed (e.g., [17], [21], [22], [23], [24], [25], [54], [55], [56], [57], [58]. However, the need to use different methods for fine- and coarse-resolution images has not been explicitly addressed, leaving a critical gap in adapting gap-filling techniques to the different characteristics of these datasets.

The second challenge lies in accurately detecting cloud-contaminated pixels, particularly thin clouds, in fine-resolution imagery. Clouds typically shows high reflectance in the visible and near-infrared bands, often resulting in abnormally bright pixels and pixels with lower brightness temperature in thermal bands. Thin clouds and shadows, on the other hand, pose unique challenges as they partially obscure the surface while allowing some radiance transmission, leading to mixed pixel values. Detected invalid pixels appear as spatial and/or temporal discontinuities in satellite imagery, often referred to as gaps or missing pixels. However, recent studies have further

highlighted the limitations of existing cloud and shadow detection methods, especially when dealing with high-resolution images. Chen et al. [59] demonstrated that while deep learning-based cloud detection, such as multiscale 3D-CNN, improves the accuracy of gap-filled pixels, it still struggles with thin clouds due to their spectral similarity to background objects such as water, mountains, and snow [59]. Similarly, Han et al. (2020) found that high-resolution shadow detection is prone to misclassification of cloud-contaminated pixels, often confusing dark non-shadow regions with actual shadows [60]. Zhang et al. [61] emphasized that many cloud removal methods rely on a single clear-sky reference image, which is often unavailable, leading to inconsistent results in high-resolution images [61]. Similarly, Lei, et al. [62] found that traditional shadow correction techniques often result in over-correction in some areas while leaving others under-corrected, leading to inconsistencies in accuracy. These studies collectively highlight the ongoing difficulty in developing automated cloud and shadow detection algorithms that can effectively handle thin cloud layers and cloud shadows while maintaining reliability in high-resolution remote sensing imagery. According to the study conducted by Wang, et al. [23], a major challenge in detecting invalid pixels in fine-resolution Landsat images stems from the limitations of Quality Assurance (QA) flagging systems. These QA systems, while providing a basic framework for identifying gaps, often fail to detect subtle anomalies such as thin clouds and shadows. To overcome this shortcoming, Wang, et al. [23] proposed a methodology that combines QA flags with thresholding techniques and visual inspection. The thresholding approach leverages spectral reflectance properties to improve the accuracy of cloud and shadow detection, thereby addressing gaps left by QA algorithms. Although their method [23], improves the identification of invalid pixels, it has notable limitations. The reliance on visual inspection, while effective in identify the undetected invalid pixels, introduces significant drawbacks. It is time-consuming and inherently non-scalable, making it unsuitable for large-scale or automated applications. This reliance on manual processes highlights the need for more automated and scalable approaches that can maintain accuracy without requiring extensive human intervention. This challenge is less pronounced for coarse spatial resolution imagery, where cloud detection algorithms generally achieve higher accuracy in identifying clouds.

This improved performance is largely attributed to their ability to leverage temporal information inherent in time-series data, which provides a richer context for detecting invalid pixels. For example, MODIS serves as a prime example of a satellite system optimized for high temporal resolution, revisiting locations daily. It employs advanced cloud detection mechanisms such as the MOD35 cloud mask and the internal MOD09 QA flags, which leverage information from multiple spectral bands alongside contextual algorithms to identify clouds and shadows [63]. The "state_1km" dataset, a critical component of the MODIS QA flags, has undergone extensive global validation to ensure reliability. Notably, these algorithms are highly effective at detecting even thin clouds, a challenge for many other remote sensing platforms. This capability significantly improves the accuracy of MODIS data in identifying invalid pixels, making it a reliable source for gap-filling methods. Additionally, the integration of temporal continuity into these algorithms further bolsters their robustness, enabling consistent performance under varying atmospheric conditions.

The third challenge is how to find valid observations to serve as primary information for gap-filling of fine spatial resolution data. Existing gap-filling methods, such as the Neighborhood Similar Pixel Interpolator (NSPI) proposed by Chen et al [54], typically rely on fixed-shape search windows to identify neighboring pixels with similar spectral characteristics. Similarly, Shen-Chuan, et al. [64] introduced a method that uses an adaptive search window combined with linear regression to restore missing pixels in remote sensing images. Their approach adjusts the size of the search window based on local image characteristics to identify suitable neighboring pixels for reconstruction. More recently, Guo, et al. [65], proposed the Class-based Linear rEgression and iterAtive Residual compensation (CLEAR) method for gap-filling of optical images. By classifying time-series reference images, CLEAR characterizes annual land-cover dynamics to guide gap-filling steps. The method preliminarily fills gaps using class-based linear regression, assuming that pixels within the same land-cover class exhibit similar temporal changes, and refines predictions through iterative residual compensation that integrates neighboring pixels' residuals. Building on the methodologies reviewed, Chen, et al. [54], advanced gap-filling techniques by introducing an adaptive search window determined through spatial autocorrelation, paired with enhanced spatial and spectral weighting. This approach dynamically optimized the search window size to ensure the inclusion of sufficient valid neighboring pixels while maintaining computational efficiency. It complements previously discussed methods, such as the fixed-shape windows of NSPI [54], and the adaptive regression windows of Shen et al., by emphasizing both local spatial relationships and spectral similarity. These innovations significantly improve the definition of pixel similarity for identifying valid observations, which serve as the foundation for fine-resolution gap-filling. However, they also highlight the need for future approaches that integrate more flexible and dynamic search strategies. By accommodating complex spatial patterns among neighboring pixels and employing diverse search window configurations, such strategies could further enhance gap-filling accuracy, particularly in challenging landscapes.

Therefore, to address aforementioned challenges, we proposed an adaptive gap-filling approach for multi-spectral satellite imagery. We introduced distinct gap-filling methods explicitly designed to optimize reconstruction for fine- and coarse-resolution imagery, separately. For images with fine-spatial resolution, our approach automatically identifies invalid pixels without relying on visual inspection. It then employs regression-based methods to reconstruct the values of the detected invalid pixels. This is achieved by dynamically utilizing varying search windows with different shapes and

orientations, effectively capturing different spatial patterns of valid observations of surface reflectance. For images with coarse spatial resolution, our approach relies on QA flags provided with the dataset to identify invalid pixels and fills the gaps by adapting to varying gap conditions. This is achieved through a combination of global regression, local regression and geo-spatial analysis, with the method selected based on the gap percentage in each image (day). The approach operates independently of auxiliary datasets, ensuring robust and reliable performance even under challenging conditions.

II. Data and Study Area

A. Fine and coarse spatial resolution satellite data

To implement and evaluate our method, we utilized two major datasets tailored for fine- and coarse-resolution images. For fine-resolution, we used atmospherically corrected surface reflectance and Land Surface Temperature (LST) from thermal infrared (TIR) data from Landsat 8 OLI/TIRS and Landsat 7 ETM+ sensors. These datasets include four visible and near-infrared bands (Blue, Green, Red, and NIR), one SWIR band, one TIR band, and the QA_PIXEL band. The QA_PIXEL band encodes pixel-level quality information related to clouds, cloud shadows, snow/ice, and water, as summarized in Table I. All available images and corresponding QA band from January 1, 2018, to December 31, 2018, for our study area (Fig. 1) were downloaded from Google Earth Engine (GEE).

For coarse spatial resolution, we used the MODIS Terra Surface Reflectance Daily Global 1 km dataset (MOD09GA, version 6.1, 10:30 AM). This dataset includes four spectral bands (Blue, Green, Red, and NIR) and the Reflectance Data State QA band (state_1km). Detailed information about the MODIS state_1km QA band is summarized in Table I. Images spanning from 2002 to 2022 were also obtained through GEE.

MODIS dataset, with the high temporal resolution of Terra satellite (daily revisit), utilizes robust cloud detection algorithms, including the MOD35 cloud mask and the QA flags in MOD09 reflectance dataset [63]. These algorithms apply multiple spectral bands and contextual tests, offering reliable cloud and shadow identification. Pixels flagged as poor quality, i.e. those affected by clouds, shadows, or other atmospheric interferences, were classified as invalid observations. In contrast, pixels marked as good quality were retained as valid observations [66].

TABLE I
QA Flags details for Landsat and MODIS Data

Dataset	QA Band	Bit	Description	Values/Meaning
Landsat	QA_PIXEL	Bit 0	Fill	0: Valid, 1: Fill pixel
		Bit 1	Dilated Cloud	0: No, 1: Yes
		Bit 3	Cloud	0: No, 1: Yes
		Bit 4	Cloud Shadow	0: No, 1: Yes
		Bit 5	Snow/Ice	0: No, 1: Yes
		Bit 7	Water	0: No, 1: Yes
		Bits 8–9	Cloud Confidence	0: None, 1: Low, 2: Medium, 3: High
		Bits 10–11	Cloud Shadow Confidence	0: None, 1: Low, 2: Medium, 3: High
		Bits 12–13	Snow/Ice Confidence	0: None, 1: Low, 2: Medium, 3: High
		Bits 14–15	Cirrus Confidence	0: None, 1: Low, 2: Medium, 3: High
MODIS	state_1km	Bits 0–1	Cloud State	0: Clear, 1: Cloudy, 2: Mixed, 3: Not set (assumed clear)
		Bit 2	Cloud Shadow	0: No, 1: Yes
		Bits 3–5	Land/Water Flag	0: Shallow ocean, 1: Land, 2: Ocean coastlines/lake shorelines, 3–7: Various water types
		Bits 8–9	Cirrus Detected	0: None, 1: Small, 2: Average, 3: High
		Bit 12	MOD35 Snow/Ice Flag	0: No, 1: Yes
		Bit 13	Adjacent to Cloud	0: No, 1: Yes
		Bit 14	BRDF Correction Performed	0: No, 1: Yes
		Bit 15	Internal Snow Mask	0: No Snow, 1: Snow

B. Study area

The area selected to test and to evaluate the method is around Zhangy oasis located in the northeast region of China, spanning approximately 1,600 km2 (Fig. 1). This area was selected due to its heterogeneous land cover, which poses unique challenges for gap-filling methods. As illustrated in Fig. 1, three highlighted regions showcase the diverse land cover types, further emphasizing the complexity of the study area. Moreover, this region frequently experiences thin clouds and shadows, which are often undetected by the QA flags, particularly in fine-resolution images. This characteristic provided an opportunity to assess the robustness of our invalid pixel identification technique (refer to section II.B.1) and ensure a thorough evaluation under demanding conditions.

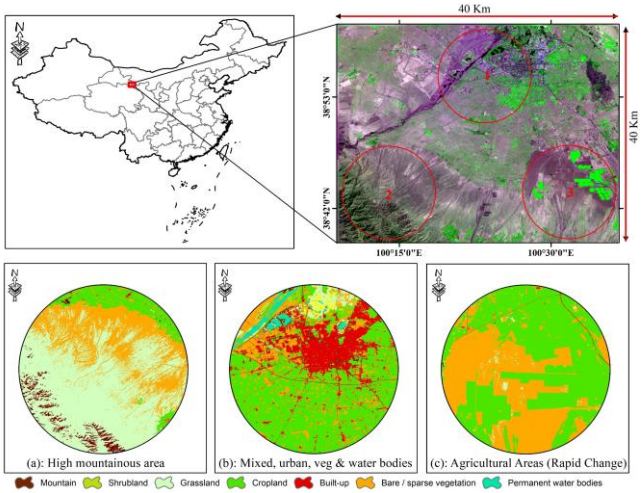

Fig. 1. The selected area for the experimental design and method testing. The red circle highlights three different land covers, which are enlarged at the bottom of the figure. Each red circle is numbered, with the corresponding view displayed as three separate squares with matching numbers. The case study area covers approximately 40 × 40 km^2.

III. Methodology

This study proposes a comprehensive gap-filling framework tailored to the distinct requirements of fine- and coarse-resolution satellite imagery. For coarse-resolution images, gaps

are identified using QA flags provided with the dataset (i.e. MODIS QA dataset in this study), where pixels with lower values are classified as invalid. The method then calculates the Missing Pixel Percentage (MPP) for the dataset and applies a threshold-based approach to determine the appropriate gap-filling technique. Depending on the MPP in the image on each day, gaps are filled using methods named as Global Regression Analysis (GRA), Local Regression Analysis (LRA), or Geo-spatial Analysis (GA).

For fine-resolution images, the process begins with thresholding techniques to identify invalid pixels, with thresholds based on quality flags (i.e. QA dataset from Landsat). For each gap pixel the gap-filling method utilizes dynamic search windows of varying shapes and sizes to adapt to spatial heterogeneity, constructing regression models from valid observations surrounding the gap pixel with valid pixel on the same position but at different times or spectral bands. The best regression model is selected by maximizing the coefficient of determination (R^2), ensuring robust reconstruction. If a suitable model is not found, the search window is redefined, and the process is repeated until the R^2 threshold is met. Any remaining unfilled pixels are handled using spatial interpolation techniques. This framework provides an effective, adaptable approach for addressing gaps in satellite imagery, ensuring reliable data reconstruction for both coarse- and fine-resolution datasets. The workflow of the proposed method is summarized in Fig. 2.

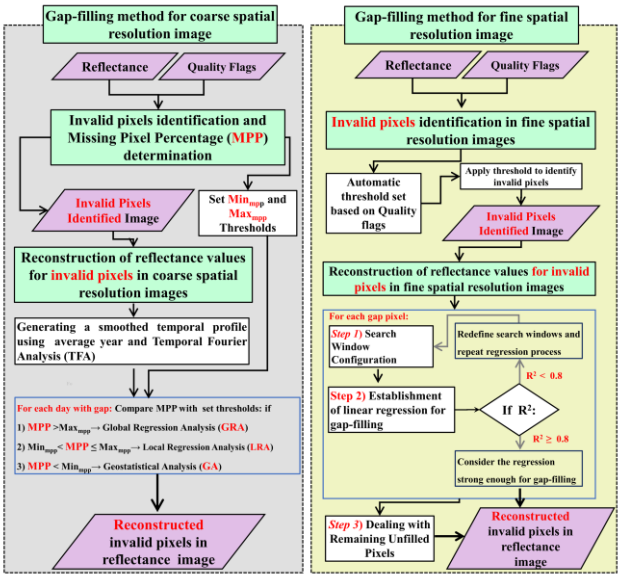

Fig. 2. The overall workflow of the gap-filling methods in this study: left panel for coarse-resolution image; right panel for fine-resolution image.

A. Gap-filling method for coarse spatial resolution image

The gap-filling approach for coarse spatial resolution images presented here is part of our broader research efforts and has been detailed in [67]. This method is developed to fill gaps in datasets with coarse spatial resolution but high temporal resolution, such as MODIS. We have successfully applied this method for fill the gaps in MODIS land surface temperature (LST) images [67]. Only brief description of the procedure will be given in this paper.

1) Invalid pixels identification and Missing Pixel Percentage (MPP) determination

The accuracy of invalid pixel identification is critical for ensuring the reliability of gap-filling processes in both fine- and coarse-resolution imagery. Invalid pixels in coarse-resolution images were identified using only the QA flags available in the MODIS data products. The straightforward approach leverages the high temporal resolution of MODIS and its robust QA flagging system to ensure effective identification of invalid pixels.

The MPP, which represents the percentage of invalid pixels relative to the total number of pixels in each image (e.g. study area), is calculated based on the QA flags in the MODIS products. Two thresholds, Min_{mpp} (i.e., the threshold for conditions with minimal gaps) and Max_{mpp} (i.e., the threshold for conditions with significant missing data), are determined based on the first and last deciles of the MPP frequency distribution from our 2002-2022 dataset. These thresholds categorize the severity of gap and guide the selection of the appropriate reconstruction method. Specifically, when the MPP is below Min_{mpp}, the method employs Local Regression Analysis (LRA) due to the availability of sufficient valid neighboring pixels. When the MPP is above Max_{mpp}, Global Regression Analysis (GRA) is applied, using broader spatial patterns for reconstruction. In intermediate cases, Geospatial Analysis (GA) is used to balance local and global information. This adaptive approach ensures optimal gap-filling efficiency under varying data loss conditions. Detailed information and parameter settings can be found in our previous work [67].

2) Reconstruction of reflectance values for invalid pixels in coarse spatial resolution images

To guide the reconstruction process, a reference year is generated. The reference year is constructed by averaging the pixel values (e.g., surface reflectance) for each day of the year (1–365) across a long time series. To ensure temporal consistency and enhance spatial continuity, Temporal Fourier Analysis (TFA) is applied to the reference year dataset [68]. This process creates a smoothed temporal profile, accounting for the unique yearly temporal pattern of each pixel. By minimizing inconsistencies in the temporal profile, TFA ensures greater spatial coherence across the dataset, which is particularly critical for maintaining the large-scale patterns of coarse spatial resolution imagery. The refined reference year serves as a robust temporal baseline for the gap-filling process. Lastly, for each daily image, the following techniques will be applied based on the previously set MPP thresholds:

Global Regression Analysis (GRA):

When a given day MPP exceeds Max_{mpp}, indicating a high number of invalid pixels, GRA is applied. This method establishes a regression model between the valid observations (pixels) across the image (image with gap which is being processed) and same pixels in the reference year image. Then applies the established regression to the pixels in the reference year at the locations of gap pixels in the current image to fill the gaps. This approach captures broad temporal trends and ensures

that the reconstructed pixels align with the overall patterns of the dataset. GRA is particularly suited for scenarios where invalid pixels are widespread, as it reconstructs data by leveraging global relationships.

Local Regression Analysis (LRA):

For moderate MPP values that fall between Min_{mpp} and Max_{mpp}, LRA is employed. This method uses a moving window approach, using a regression between valid pixels in the spatial vicinity of the invalid pixel and the corresponding pixels in the reference year. The moving window dynamically adjusts its size to include sufficient valid observations, ensuring reliable reconstruction.

Geo-spatial Analysis (GA):

When the MPP is below Min_{mpp}, indicating sparsely distributed invalid pixels, GA is applied. This method leverages Tobler's First Law of Geography, which states that closer entities are more related than distant ones. This principle underpins the use of neighborhood information and spatial analysis to reconstruct missing pixels, particularly when gap sizes are relatively small. In this approach, the reference image, corresponding to the same day of year (DoY) as the image being initially gap-filled, is segmented using the *K*-means clustering algorithm with *K* set to 5 to assign a class to each gap pixel. The decision to use $K = 5$ in the *K*-means clustering algorithm was guided by prior research [17], [69] applied this method to gap-filling tasks. These studies indicated that an optimal *K* typically falls within the range of 3 to 7, which has been shown to work effectively for such applications. As a result, we chose the midpoint of this range as the fixed value for *K* in our study. Then the 10 nearest pixels within the same class are selected to calculate the weighted average of these pixels, with weights inversely proportional to their distance from the target pixel, ensuring closer pixels contribute more to the estimation.

B. Gap-filling method for fine spatial resolution image

A reconstruction method to fill values of the invalid pixels is proposed to alleviate the spatial discontinuity or identified invalid pixels in fine-resolution images. The core of this method is the correlation between valid observations surrounding a target gap pixel and those at the same spatial location but from different times and spectral bands. This process applies search windows of different shapes and sizes to explore different configurations of valid observations. The relationships are quantified by linear regression, with the equation with the highest R^2 selected for gap-filling. In addition, a predefined correlation coefficient threshold (set to 0.8 in this study) ensures that only robust regression equations contribute to the reconstruction of the value in the gap pixel, thereby minimizing errors. If the initial equations do not meet the threshold, or if there are insufficient valid observations for a regression model, the size of the search window is incrementally increased. This adjustment continues until the threshold conditions are met or the window size reaches the image dimensions. In scenarios where a few pixels remain unfilled, interpolation methods using nearby valid observations are applied to fill these remaining gaps in step 3. The detailed technical implementation of our method is explained in the following sections.

1) Invalid pixels identification in fine spatial resolution images

The fine-resolution datasets, for example Landsat images, with their lower temporal frequency (16-day revisit), rely on simpler QA flags that are less effective in detecting thin clouds and shadows [23], [70]. An example of this failure is shown in Fig. 3. This inadequacy necessitates supplementary threshold-based methods to identify undetected invalid pixels, especially in heterogeneous landscapes where cloud detection is more challenging. Hence, we combined the QA flags with a thresholding technique to detect additional invalid pixels.

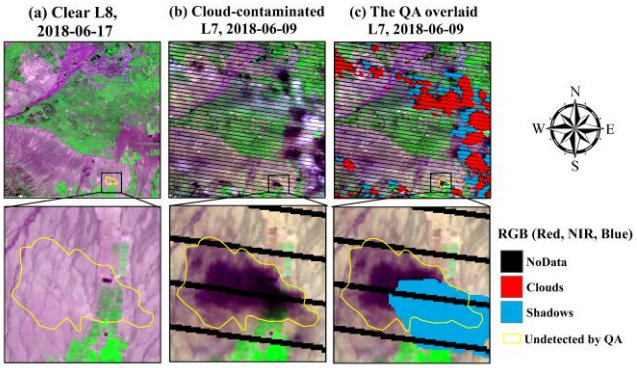

Fig. 3. An example of effectiveness of the Landsat QA layer in identifying cloud-affected pixels. The upper row (from left to right) shows: a clear Landsat 8 image (dated 2018-06-17, near the next cloudy Landsat 7 acquisition), a cloud-contaminated Landsat 7 image, and a Landsat 7 image overlaid with the QA layer highlighting clouds and shadows. The lower row presents a zoomed-in view of the same images.

To implement our technique, we selected the blue, near-infrared (NIR), and shortwave-infrared (SWIR) spectral bands, which are particularly effective in detecting shadows [70], [71]. Additionally, a thermal infrared (TIR) band was applied to identify clouds [72]. These bands were selected because shadows and clouds exhibit characteristic spectral signatures in these spectral ranges, making them ideal for distinguishing invalid pixels from valid observations.

To establish thresholds for identifying clouds and shadows, the method first examines the pixels in a given image, in particular the ones flagged by the QA as clouds or shadows. Baseline thresholds are estimated by calculating the average pixel values for these flagged pixels in each of the selected bands. These thresholds serve as reference values for identifying other potentially invalid pixels.

Once the thresholds are set, the method evaluates each pixel in a given image. If a pixel values in all three spectral bands fall below the shadow thresholds, it is flagged as a shadow pixel. Likewise, if a pixel value in the thermal band is below the cloud threshold, it is flagged as a cloud pixel. This process ensures that pixels potentially missed by the QA flags are identified and labeled correctly.

To avoid misclassification, the method specifically excludes water, ice, and snow pixels from being flagged as clouds or shadows. These exclusions are informed by the original QA flags and supplemented by spectral indices like the Normalized

Difference Snow Index (NDSI) and Normalized Difference Water Index (NDWI), which reliably distinguish water and snow/ice from other surface features [73], [74], [75], [76], [77]. The reliability of Landsat QA for water, ice, and snow stems from their distinct spectral signatures in VNIR and thermal bands, which are well-captured by the QA algorithms. The detailed workflow for identifying invalid pixels in fine spatial resolution images is outlined in Fig. 4.

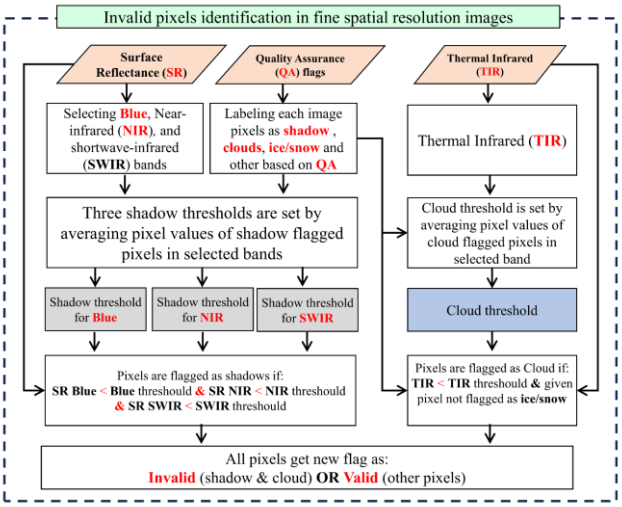

Fig. 4. Detailed workflow for identifying invalid pixels in fine spatial resolution images. Critical parameters are highlighted in bold and red.

2) Reconstruction of reflectance values for invalid pixels in fine spatial resolution images

The following steps give the details of reconstruction of reflectance values for invalid pixels in fine-resolution image.

Step 1) Configuration of the search windows

To effectively reconstruct each missing pixel, we apply search windows that vary in shape, size and orientation (Fig. 5). This variation maximizes the extraction of relevant information for reconstructing the missing pixels. The design of these windows is important as they are used to capture the distribution of valid observations in the neighborhood of each gap. The dimensions of a search window are (v, u), where v is the number of columns and u is the number of rows. In this study, the initial size of each window is set to (9, 9) for a square window and (9, 5) or (5, 9) for rectangular windows, as these dimensions were found to be the most effective based on preliminary trial-and-error analyses. To set a directional search window for gap-filling in fine spatial resolution images, we retain a square-shaped search window but selectively utilize valid pixels along two specific diagonal directions. The selected pixels follow either (1) an upper-left to lower-right direction or (2) an upper-right to lower-left direction. Only the pixels along the selected diagonal direction within the search window are used for regression. Fig. 5 illustrates these directional configurations. For directional windows, the size remains the same as for the square shape, but the orientation of the pixels is different. If the number of valid observations in either setting is less than 75% of the window size ($v \times u$), the window size is incrementally increased.

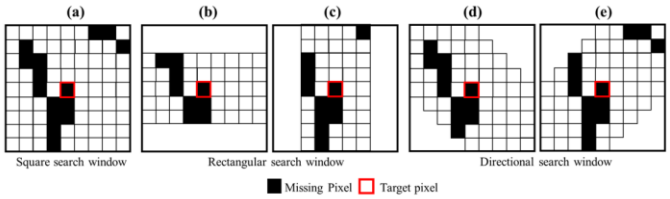

Fig. 5. Configurations of a search window. (a): square Shape, (b) and (c): rectangular and (d) and (e): directional shape. Black: missing pixels; red board: target missing pixel to be filled.

Step 2) Establishment of linear regression for gap-filling

Assuming that the pixels close to each other have similar spatial and temporal characteristics, a separate linear regression of the pixel reflectance for each band (λ) between two paired windows, one in the target image on day t_1, where gaps need to be filled, and one from another image on any different day (t_2), can be established. The reflectances in the available pixel pairs at the same location in the two paired-image windows are used to estimate the unary linear regression as:

$$Y_{t_1, w_m, \lambda_k} = a_{t_{1,2}, w_n, \lambda_h} + b_{t_{1,2}, w_n, \lambda_h} \cdot Y_{t_2, w_n, \lambda_h} \quad (1)$$

where Y_{t_1, w_m, λ_k} is the reflectance on day t_1 in band λ_k in the available pixels in window w_m, i.e. $Y_{t_1, w_m, \lambda_k} \in \{\rho_{t_1, w_m, \lambda_k}(i_1, j_1), \rho_{t_1, w_m, \lambda_k}(i_1, j_2), \dots\dots, \rho_{t_1, w_m, \lambda_k}(i_I, j_J)\}$; Y_{t_2, w_m, λ_h} is the reflectance array on day t_2 for each band λ_k at the same locations of Y_{t_1, λ_k, w_m}, i.e. $Y_{t_2, w_m, \lambda_h} \in \{\rho_{t_2, w_m, \lambda_h}(i_1, j_1), \rho_{t_2, w_m, \lambda_h}(i_1, j_2), \dots\dots, \rho_{t_2, w_m, \lambda_h}(i_I, j_J)\}$. λ_k and λ_h are the spectral band indicators ranging from blue, red, green and to NIR bands of Landsat (k can be equal to h); w_m (and w_n) is indicator for a search window in the set with m (and n) = 1, 2, …,5 as indicated in Fig. 5 (m can be equal to n). $a_{t_{1,2}, w_m, \lambda_{k,h}}$ and $b_{t_{1,2}, w_m, \lambda_{k,h}}$ are regression coefficients estimated from least square fit.

For each gap pixel in band k, in total 20 (= 5 window shapes x 4 bands) different linear regressions with the R^2 values can be established. A $R^2 > 0.80$ indicates a valid regression to fill the invalid pixels. The linear regression with the highest R^2 value, denoted as window w_X and band λ_H, is selected to calculate the value in the gap pixel using:

$$\rho_{t_1, w_x, \lambda_k}(i_0, j_0) = a_{t_{1,2}, w_X, \lambda_H} + b_{t_{1,2}, w_X, \lambda_H} \cdot \rho_{t_2, w_X, \lambda_H}(i_0, j_0) \quad (2)$$

where $a_{t_{1,2}, w_X, \lambda_H}$ and $b_{t_{1,2}, w_X, \lambda_H}$ are the coefficients taken from the linear regression with the highest R^2 obtained from the previous step, $\rho_{t_1, w_x, \lambda_k}(i_0, j_0)$ is the filled value of reflectance of band λ_k in window w_x in the gap position (i_0, j_0) on day t_1, $\rho_{t_2, w_X, \lambda_H}(i_0, j_0)$ is the reflectance of band λ_H with window shape w_X (corresponding to the regression with the maximum R^2) at the same location (i_0, j_0) on day t_2.

If the number of valid observations in either set is less than 75% of the window size (Column × Row), the search window size is incrementally increased and the regression process is repeated to seek for better results. This step is crucial for

gathering enough valid observations to establish a reliable regression.

If the R^2 value still remains below 0.80 after the search window has reached the size of the full image, we apply an alternative procedure (step 3).

Step 3) Dealing with remaining unfilled pixels:

The foundation of our procedure to reconstruct the remaining unfilled pixels is based on the fundamental principle of geography, as articulated by Tobler [78], which suggests that all entities are interconnected, but the degree of their relationship reduces with increasing spatial distance. Taking into account this fundamental principle, our objective is to reconstruct the pixels that cannot be filled using the regressions described above by using the nearest similar valid pixels. These pixels are identified by applying image segmentation to the image [17] closest in time to the date of the image being processed. The segmentation was performed using the *K*-means clustering algorithm, with *K* set to 5 (see section III.A.2). This algorithm categorizes the image into five distinct clusters. After determining the class of the target invalid pixel, we select the ten nearest pixels within the same class as reference pixels. The values at the missing pixel are then estimated as a weighted average of the reference pixels [79], where weights depend on the distance, giving higher weights to closer pixels.

C. Experimental design for method evaluation

To evaluate the performance of the proposed gap-filling method and its robustness under diverse conditions, two experiments were conducted. The experimental design included two main components: 1) assessing the accuracy of the gap-filling process for both fine- and coarse-resolution images using artificially introduced gaps; 2) evaluating the identification of invalid pixels and its impact on gap-filling performance for fine-resolution images. These experiments were designed to systematically explore how different factors, such as error rates in invalid pixel identification and the size and spatial distribution of gaps, affect the method's effectiveness.

1) Evaluation of gap-filling performance using artificially introduced gaps

Artificially introduced gaps are a primary method to evaluate the gap-filling performance for both coarse and fine-resolution images. This experiment was designed to assess how the percentage and position of gaps affected gap-filling accuracy. For this purpose, a clear image was selected, and three scenarios were considered: randomly introduced gaps with real cloud and shadow shapes (Fig. 6a), centrally introduced growing gaps (Fig. 6b), and corner-introduced growing gaps (Fig. 6c). The gap percentages varied from 10% to 90% of the total image area in these scenarios (Fig. 6), randomly positioned gaps mimic cloud and shadow shapes and are distributed throughout the image at different percentages. The central gaps were introduced as a circular shape expanding from the center of the image (Fig. 6, middle panel), while the corner gaps expanded from the top left of the image (Fig. 6, lower panel). To evaluate the gap-filling method using these gap-introduced images, the method was applied to each image, and the reconstructed reflectance of artificial gap pixels were compared with the original values from clear pixels. Performance metrics, as outlined in section. II.C.3, were then calculated to assess the method accuracy.

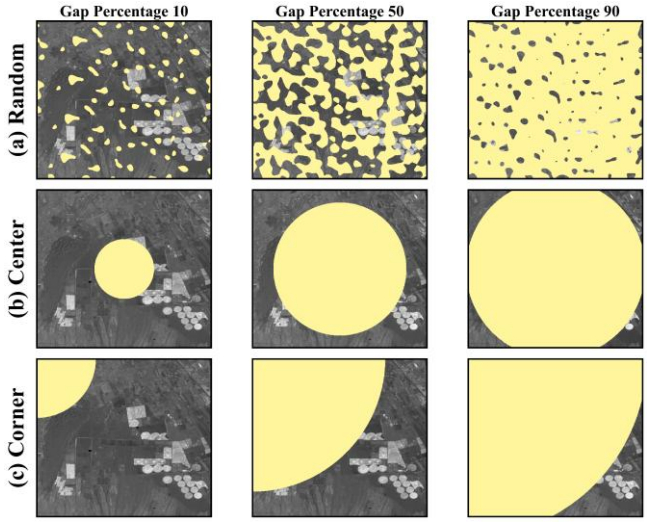

Fig. 6. Different types of artificially introduced gaps (yellow color). (a), (b) and (c) are for artificial gaps generated by random, center and corner distributions, respectively. Each row indicates the percentage of gaps ranging from 10% to 90% (here only middle (50%) and extreme (10% and 90%) cases were represented).

2) Impact of QA errors on invalid pixel identification and gap-filling in fine spatial resolution images

To evaluate the impact of QA errors on invalid pixel identification and gap-filling for fine-resolution images, an experiment was conducted. Our method (Section III.A.2) relies on QA flags to set thresholds to identify clouds (using LST) and shadows (using reflectance), inconsistencies between QA flags and the actual conditions can affect the identification of invalid pixels. For instance, a QA layer that incorrectly flags valid observations as invalid will results in higher thresholds and a larger number of pixels being classified as invalid over the study area, which will improve the quality of the remaining valid pixels. To evaluate the on gap-filling performance, we designed an experiment using artificially generated images and QA layers (Table II).

For each spectral band an artificial cloud-contaminated image was generated by combining a clear-sky with a contaminated image acquired several days apart. Visual inspection of the contaminated image was first performed separately for the Blue, NIR SWIR and TIR bands to preliminarily select the areas contaminated by either shadows or clouds. The initial thresholds for identifying either shadow or cloud pixels were estimated by averaging the corresponding band reflectance (or LST) for these visually detected pixels. This gave the shadow thresholds of 0.06 for the blue, 0.15 for the NIR and 0.1 for the SWIR band, with a cloud threshold of 243K for the TIR band. Furthermore, the pixels below these thresholds in the contaminated images were marked as either shadow or cloud pixels, and the reflectance or LST values in these pixels in the clear-sky images were then replaced with the

reflectance or LST values from the contaminated image. This created the artificial contaminated images in different bands and an artificial QA layer (with clear, shadow and cloud flags) for further analysis.

To analyze the impact of QA errors on the gap-filling performance, two scenarios were simulated and evaluated by manipulating the QA flags in the artificial QA layer created early:

a) Failure in the QA: This is the situation where the pixels were either shadow or clouds, but marked as "clear" by the QA flag. 50% of the pixels flagged as cloud and shadow were randomly reclassified as clear pixels without changing the reflectance values. This created a new artificial QA layer containing the pixels that were not detected as invalid pixels.

b) Errors in the QA: This is the situation where the pixels were clear-sky, but marked as either shadow or cloud by the QA flag. In addition to the 50% undetected pixels, varying error rates between 5% and 50% (with 5% interval) of the cloud and shadow pixels initially identified by the artificial QA layer, were introduced; new images incorporating these varying errors were created by randomly replacing the clear-sky labels This introduced increasing level of errors into the artificial QA layer created in the previous step of this section.

Each artificially manipulated QA layer was input into our invalid pixel identification method, leading to increasing threshold values and subsequent pixel identification. The gap-filling method was then applied based on these identifications to evaluate the impact of varying QA errors on gap-filling performance.

For clarity, each experiment was labeled sequentially, and the details of all experiments are presented in Table II.

TABLE II

EXPERIMENTAL DESIGN FOR EVALUATION OF THE GAP-FILLING METHOD FOR HIGH SPATIAL RESOLUTION IMAGE BY GENERATING ARTIFICIAL CONTAMINATED IMAGES AND QA LAYERS.

Experiment no.	Experiment Configuration
Exp. 0	Baseline scenario, where the gap-filling method was applied directly to the pixels labeled as shadow and cloud in the QA layer with 50% failure, without utilizing our invalid pixel identification method
Exp. 1	Using the QA with 50% failure as input to our invalid pixel identification method
Exp. 2	Using the generated artificial QA with both 50% failure and 5% error as input
Exp. 3 – Exp. 11	As Exp. 2 but error rates in the QA layer increasing from 10% to 50% in 5% increments

3) Evaluation Metrics:

Four common indicators were used to evaluate the method performance. The Root Mean Square Error (RMSE) and Mean Absolute Error (MAE) measure the difference between predicted and actual values. The Structural Similarity Index Measure (SSIM) measures texture similarity of the reconstructed pixels, focusing on the preservation of structure, contrast, and brightness from the valid pixels. Higher SSIM values indicate better retention of image details. Lastly, the R^2 evaluates the relationship between predicted and actual data, with higher values reflecting greater accuracy in estimating relative pixel values. For detailed formulations of these indicators, refer to [80].

IV. RESULTS

We will present the results of the study in two main sections. Section IV.A presents the results for the coarse-spatial resolution image and Section IV.B shows the results for the fine-resolution observation, each section includes gap identification and gap filling and highlights the key issues to be addressed.

A. Evaluation of gap-filling results for coarse-spatial resolution image

1) Invalid pixels identification and reconstruction in coarse spatial resolution images

The identification and reconstruction of invalid pixels in coarse resolution images were carried out as described in Sect. III.A.1 and III.A.2. In the original image (Fig. 7a), clouds and shadows are clearly distinguishable by their bright and dark appearances, respectively. Fig. 7b shows the pixels identified as invalid using the QA flags from MOD09A dataset. A visual comparison between the gapped image (Fig. 7b) with the original image (Fig. 7a) confirms that the QA flags effectively captured potentially invalid pixels, demonstrating their reliability in identifying clouds and shadows in coarse-resolution images. This assessment is based on the alignment between QA-flagged pixels and visually identified invalid pixels, as illustrated in Fig. 7a and b. The accuracy of QA flags in coarse-resolution data, such as MODIS, has also been documented in previous studies [81], [82], which documented the performance of the QA in MOD09A in detecting invalid pixels under various conditions. Fig. 7c displays the gap-filled image on the same day, illustrating the reconstruction of the identified invalid pixels. Visual inspection reveals no noticeable discontinuities between the pre-existing valid observations and the reconstructed pixels.

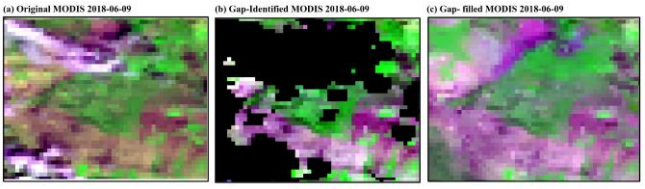

Fig. 7. Original (a), gapped (b) and gap-filled (c) MODIS reflectance images for 2018-06-09 (RGB is composed using red, NIR and blue bands of MODIS surface reflectance from MOD09A).

2) Gap-filling performance using artificially introduced gaps for coarse spatial resolution image

To evaluate the gap-filling method for coarse-resolution image, random gaps at various fractional abundances were

introduced in a selected clear image on 2018-08-22 (Fig. 7a). Our technique, described in Section III.A.2, was then applied to reconstruct reflectance values for these gaps. Error metrics, were calculated by comparing the reflectance values of reconstructed pixels with the reflectance of the corresponding original pixels. As shown in Fig. 8a, the RMSE values for the blue band range from 0.004 to 0.03 as the fractional abundances of gaps increase from 10% to 90%. The highest RMSE values were observed in the NIR band, ranging from 0.011 to 0.05 over different gap abundances. A similar trend is seen in the MAE values, where rising MAE values correspond to the increasing gap fractional abundances (Fig. 8b). Structural analysis using the SSIM index demonstrates that the method effectively reconstructs missing pixels while maintaining structural similarity across all bands (Fig. 8c). SSIM values range from approximately 0.96 to 0.73 as the gap percentage increases from 10% to 90%. In summary, these evaluation results show that the method achieves good accuracy in reconstructing values of invalid pixels across the analyzed spectral bands.

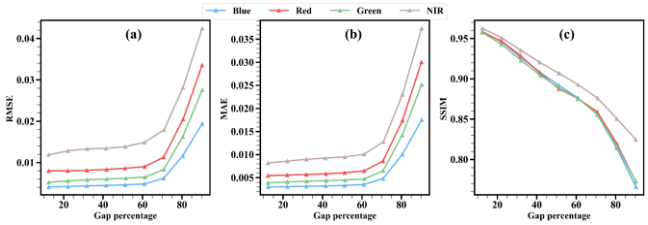

Fig. 8. Assessment of invalid pixel reconstruction in coarse-resolution images with various artificially introduced random gaps at different percentages (refer to Fig. 6a) for the reflectance of blue, red, green, and NIR spectral bands. The left panel illustrates RMSE, the middle panel depicts MAE, and the right panel shows SSIM, comparing the original to the reconstructed images.

The good reconstruction performance up to a 90% gap fraction and the remarkably stability up to a gap fraction of 60% (Fig. 9) is explained by the similarity in the reflectance distribution in the remaining clear-sky pixels (Fig. 9). The latter implies that the clear-sky pixels used to reconstruct the gaps in each image follow a rather similar frequency distribution, notwithstanding the large difference in gap fraction. This highlight robustness of the gap-filling approach across varying gap levels.

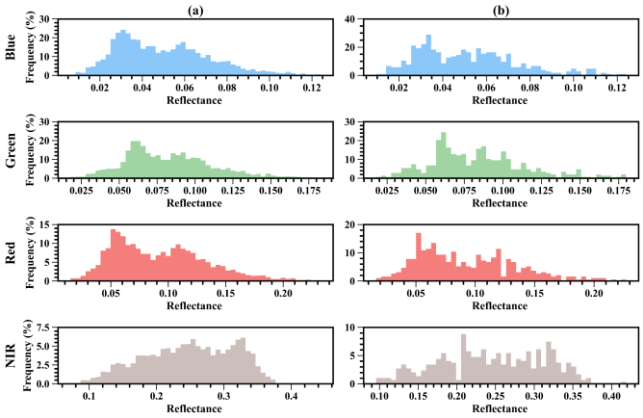

Fig. 9. Histograms of clear-sky pixel value distributions of random gaps introduced images for case 10% (a) and 90% (b) gaps in the four spectral bands (Blue, Red, Green, and NIR).

B. Evaluation of gap-filling results for fine spatial resolution image

1) Invalid pixels identification and reconstruction in fine spatial resolution images:

According to Section III.B.2 (step 3), reconstructing each identified invalid pixel requires selecting the optimal regression equation between data pairs within a specified search window for each spectral band. This separate processing is essential because the regression equations differ across spectral bands, even when the spatial configuration of the search window remains constant. For instance, consider a fixed search window of 51 × 51 pixels and the task of reconstructing an invalid pixel at row i and column j. The correlation between valid observations surrounding the missing pixel and the corresponding valid observations on a different date at the same location varies across spectral bands, resulting in different coefficients of determination, intercept and slope for each band. Consequently, a regression equation optimized for gap reconstruction in one spectral band cannot be directly applied to another, as each band exhibits unique spatial correlations within the same search window (Fig. 10). Detailed information on the regression equations, including their slopes and intercepts, for each spectral band is provided s in Table III.

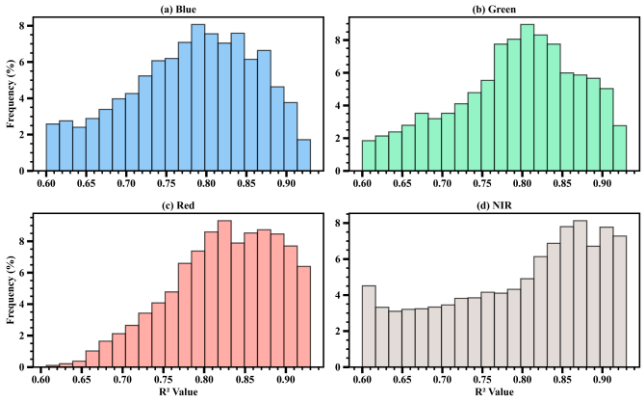

Fig. 10. Histogram of the coefficient of determination (R^2) values for regression models constructed between valid observations surrounding random missing pixels within a 51 × 51-pixel window and valid observations at the same locations but from the closest available date to the target image. The results are presented for four spectral bands: (a) Blue, (b) Green, (c) Red, and (d) NIR. Each histogram uniquely colored and titled according to the specific spectral band.

TABLE III

REGRESSION EQUATION DETAILS, INCLUDING SLOPE AND INTERCEPT, FOR 15 RANDOMLY SELECTED GAP PIXELS. THESE EQUATIONS WERE CONSTRUCTED BETWEEN VALID OBSERVATIONS SURROUNDING EACH MISSING PIXEL WITHIN A 51 × 51-PIXEL WINDOW AND CORRESPONDING VALID OBSERVATIONS FROM THE CLOSEST AVAILABLE DATE TO THE TARGET IMAGE. THIS TABLE COMPLEMENTS FIG. 10 BY PROVIDING QUANTITATIVE INSIGHTS INTO THE VARIABILITY OF REGRESSION

EQUATIONS ACROSS FOUR SPECTRAL BANDS: BLUE, GREEN, RED, AND NEAR-INFRARED (NIR).

Position		Blue			Green			Red			NIR		
I	J	R^2	interce pt	slope	R^2	interce pt	slope	R^2	interce pt	slope	R^2	interce t	slope
3	159	0.80	0.01	0.84	0.78	0.02	0.81	0.82	0.02	0.81	0.72	0	0.87
4	157	0.81	0	0.86	0.78	0.01	0.84	0.82	0.02	0.84	0.74	-0.01	0.92
16	132	0.78	0.01	0.8	0.78	0.02	0.78	0.83	0.02	0.8	0.67	0	0.87
50	161	0.71	0.02	0.76	0.72	0.03	0.75	0.76	0.03	0.75	0.71	0	0.89
53	448	0.71	0.01	0.76	0.68	0.02	0.73	0.74	0.02	0.73	0.61	0	0.82
53	457	0.74	0.01	0.71	0.74	0.02	0.72	0.79	0.02	0.73	0.62	0	0.85
54	486	0.82	0.02	0.67	0.85	0.03	0.66	0.89	0.03	0.66	0.67	0	0.86
56	205	0.73	0.02	0.7	0.75	0.03	0.71	0.77	0.04	0.72	0.64	0.06	0.68
163	231	0.81	0	0.89	0.86	0.01	0.88	0.88	0.01	0.87	0.91	0.02	0.87
233	87	0.7	0.02	0.78	0.73	0.03	0.76	0.76	0.04	0.75	0.81	0.05	0.75
235	33	0.91	0	0.85	0.9	0.01	0.81	0.92	0.01	0.84	0.84	0.01	0.84
415	322	0.72	-0.02	1.1	0.68	-0.01	1.05	0.64	0.01	0.9	0.69	0	0.95
476	432	0.83	-0.01	0.94	0.86	-0.02	0.96	0.86	-0.02	0.97	0.83	-0.01	0.9
478	96	0.75	0	0.95	0.8	0	0.95	0.82	0.01	0.93	0.82	0.01	0.93
502	68	0.83	0	0.94	0.86	0	0.98	0.87	0	0.98	0.87	-0.01	1.01

The results of identification and reconstruction of invalid pixels in fine-resolution images were shown in Fig. 11. The method successfully identified most invalid pixels (see Fig. 3), although some valid pixels were misidentified as invalid due to their low reflectance values, which closely resembled shadows, particularly in the top-center region (Fig. 11 (b)). These pixels were subsequently reconstructed as described in Sect. III.B.2. A pairwise comparison between the gapped-image (middle row of Fig. 11) and the gap-filled image (bottom row of Fig. 11) indicates that the method effectively preserves spatial continuity, with no apparent artifact. Minor reconstruction errors are visible in the enlarged view (column no. 3 in Fig.11). Despite this, the method achieved highly satisfactory results, especially in urban areas (column no.1 in Fig. 11).

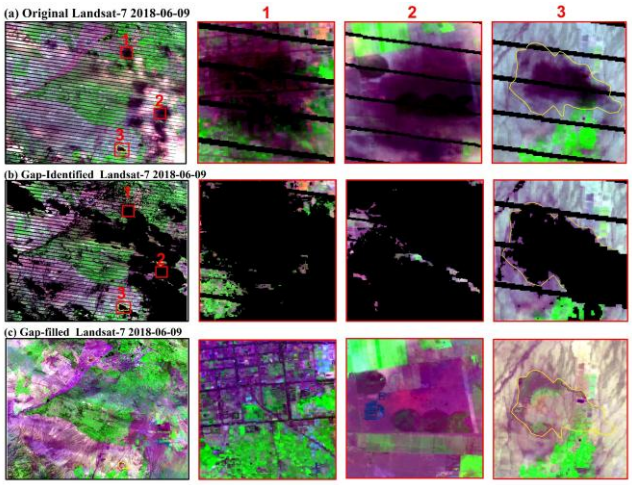

Fig. 11. Original (top-row), gap-identified (middle row), and gap-filled (bottom row) Landsat-7 images from 2018-06-09, presented as an RGB composite using the red, NIR, and blue bands. The red squares highlight three regions of interest. Enlarged views of these regions (1, 2, and 3) are displayed in the second to fourth columns on the right. Each column includes the original image (top), gap-identified image (center), and gap-filled image (bottom). The yellow polygons in region 3 indicate the hypothesized gap locations in the original, gapped and gap-filled images (see Fig. 3).

2) Gap-filling performance using artificially introduced gaps for fine spatial resolution image

Artificial gaps were introduced and gap-filling of fine-spatial images was evaluated (Fig. 11). This was done as shown in the first row of Fig. 6 and described in section III.B across four spectral bands: blue, green, red, and NIR. The method performance (Fig.12) remained relatively constant from 10% to 60% gap fractional abundance. However, performance begins to decline as gap abundance increases from 70% to 90%. The greatest errors in reconstruction were observed in the NIR band, while the blue band exhibited the least errors. Following NIR, the red and green bands showed the second and third highest errors, indicating slightly lower performance in gap-filling. Specifically, RMSE and MAE values for the NIR band ranged from 0.014 to 0.048 and 0.011 to 0.028, respectively, as the gap abundance increased from 10% to 90%. At a 60% gap abundance, these metrics were 2% and 1.4%, respectively. The SSIM followed a similar trend. For instance, at a 10% gap abundance, SSIM values were approximately 0.91 for the blue band and 0.88 for the green band, while the red and NIR bands gave 0.87 and 0.86, respectively. At a 60% gap percentage, SSIM values remained relatively similar across all bands. However, at a 90% gap percentage, structural similarity between reconstructed and actual pixels decreased significantly, with SSIM dropping to 0.70 for the red and NIR bands and to 0.75 and 0.81 for the green and blue bands, respectively.

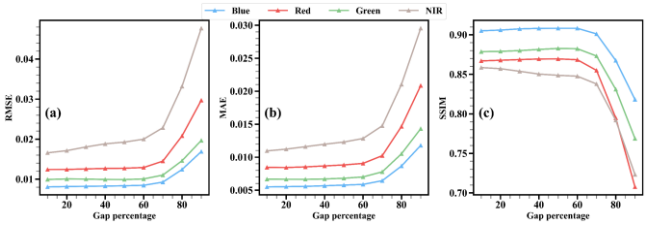

Fig. 12. Evaluation of invalid pixel reconstruction in fine-resolution images across various artificially introduced random gaps at different percentages (see Fig. 6 (a)) for the reflectance of blue, red, green, and NIR spectral bands. The left plot displays RMSE, the middle plot shows MAE, and the right plot presents SSIM, all calculated between the actual images and the gap-reconstructed images.

The spatial distribution of regression factors for invalid pixel reconstruction in fine-resolution images with 50% artificially introduced center gaps is illustrated in Fig. 13. These factors provide insight into the performance of the selected regression equations for gap-filling. Additionally, the pixel-level comparison highlights the degree of agreement between the reconstructed values and the actual reference values.

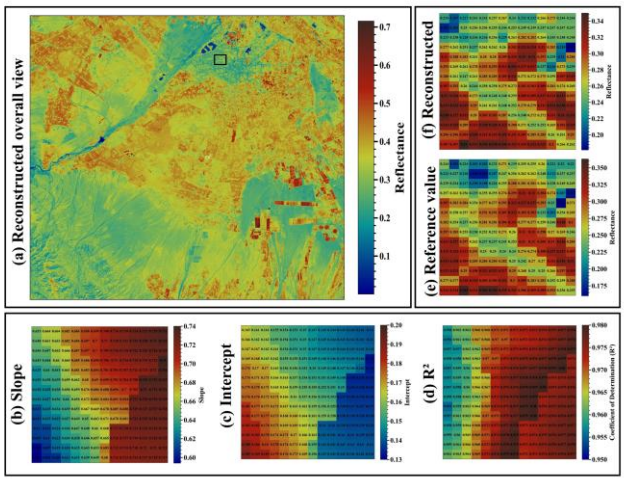

Fig. 13. Spatial distribution of regression factors for invalid pixel reconstruction in fine-resolution images for the experiment with 50% artificially introduced center gaps (see Fig. 6b) in the NIR reflectance image. (a) Overall view of the reconstructed image. (b – d) Regression factors: slope, intercept, and R2, respectively. (e, f) Pixel-level comparison between reconstructed values and actual reference values.

To further evaluate fine-resolution image gap-filling, additional artificial gaps were introduced, with gap positions specifically considered (see section III.B and Fig. 6, (b) and (c)). The results of this experiment are presented in Table IV. Overall, the results indicate that as the gap abundance increases, gap-filling performance tends to decrease slightly, particularly for corner-expanding gaps compared to center-expanding gaps. For example, at a 10% gap abundance, the RMSE and MAE for center gaps were 0.015 and .012, respectively, with the highest R^2 and SSIM values being 0.88 and 0.94. For the same gap abundance of corner gaps, the RMSE and MAE were slightly higher at 1.69% and 0.0 124, while R^2 and SSIM values were slightly lower at 83% and 82%, respectively. For mid-range abundances, i.e. 20% to 80%, the performance of gap-filling decreased overall as gap percentage increased. For instance, at a 50% gap percentage, the evaluation metrics (RMSE, MAE, R^2, and SSIM) were 0.031, 0.02, 0.83, and 0.80, respectively. In contrast, for corner gaps at these same percentages, the metrics were 0.03, 0.02, 0.80, and 0.63, indicating lower performance than center-expanding gaps.

TABLE IV

EVALUATION METRICS COMPARING RECONSTRUCTED PIXELS IN ARTIFICIALLY INTRODUCED GAPS (RANDOM GAPS IN THE SECOND COLUMN, CENTER GAPS IN THE THIRD COLUMN AND CORNER GAPS IN THE FOURTH COLUMN) WITH THE ORIGINAL PIXELS ACROSS VARYING GAP PERCENTAGES FOR THE NIR BAND. THE ORIGINAL CLEAR IMAGE WAS ACQUIRED ON 2019-05-03.

Gap	Random Gaps				Center Gaps				Corner Gaps			
%	RMSE	MAE	SSIM	R^2	RMSE	MAE	SSIM	R^2	RMSE	MAE	SSIM	R^2
10	0.0163	0.0108	0.8589	0.9115	0.0150	0.0120	0.885	0.944	0.017	0.012	0.824	0.833
20	0.0170	0.0112	0.8588	0.9008	0.0164	0.0125	0.877	0.905	0.018	0.013	0.853	0.728
30	0.0179	0.0115	0.8546	0.894	0.0182	0.0166	0.854	0.844	0.020	0.014	0.840	0.712
40	0.0198	0.0121	0.8475	0.8783	0.0341	0.0191	0.844	0.775	0.031	0.020	0.775	0.677
50	0.0183	0.0122	0.8492	0.8999	0.0311	0.0198	0.838	0.803	0.030	0.020	0.800	0.627
60	0.0204	0.0126	0.8483	0.8804	0.0320	0.0205	0.832	0.765	0.035	0.024	0.781	0.638
70	0.0199	0.0132	0.8472	0.8887	0.0345	0.0202	0.830	0.728	0.040	0.024	0.795	0.620
80	0.0216	0.0145	0.8543	0.8733	0.0314	0.0199	0.834	0.765	0.035	0.024	0.782	0.621
90	0.0624	0.0381	0.7506	0.8419	0.0355	0.0254	0.827	0.718	0.032	0.023	0.792	0.673

3) Invalid pixel identification and its impact on gap-filling in fine spatial resolution images based on the designed experiments:

In previous sections, we qualitatively illustrated the results of the method's implementation on fine- and coarse-resolution images. In this section, to evaluate the method's performance quantitatively, a series of experiments were conducted using artificially created gaps (varying in size and position) and QA applied to clear images. Performance metrics were then calculated by comparing the reference clear-sky images with the reconstructed ones.

Detailed experiments were conducted (section II.C.2) using an artificially created QA layer (Table V). In Exp. 0, where the QA layer alone was used to identify invalid pixels without any threshold adjustments, the MPP was 11.2%. In Exp. 1, thresholds were applied to identify clouds and shadows: the cloud threshold was set at 244.6 K (TIR band), while the shadow thresholds were set at 0.061 for the blue band, 0.18 for the NIR band, and 0.12 for the SWIR band, based on the invalid pixel identification technique (section III.B.1). This approach yielded an MPP of 15.1%. From Exp. 2 to Exp. 11, as the error increased, i.e. valid observations were mistakenly labeled as invalid in the QA layer), the thresholds and consequently the MPP also increased. For example, at a 5% error (section III.C.3), the cloud threshold was adjusted to 246.1, while the shadow thresholds were 0.0616 for the blue band, 0.1904 for the NIR band, and 0.1278 for the SWIR band. At a 50% error rate, these thresholds increased to 254.4, 0.0628, 0.2129, and 0.1543, respectively, with the MPP reaching 36.4%.

TABLE V

IMPACT OF ERRORS IN QA ON THE INVALID PIXEL IDENTIFICATION FOR DIFFERENT EXPERIMENTS (SECT. C.2). IN THIS METHOD, SHADOW THRESHOLDS APPLY TO THE BLUE, NIR, AND SWIR BANDS, WHILE THE TIR BAND IS USED AS THE CLOUD THRESHOLD. THE MISSING PIXEL PERCENTAGE (MPP) INDICATES THE PROPORTION OF IDENTIFIED INVALID PIXELS RELATIVE TO THE TOTAL NUMBER OF PIXELS IN THE IMAGE. EACH EXPERIMENT IS DENOTED BY THE SHORT NOTATION 'EXP. NO'. MORE DETAILED IN-FORMATION ABOUT THE EXPERIMENTAL DESIGN CAN BE FOUND IN SECTION C.2

		Shadow threshold value			Cloud threshold value	
Experiment	**QA Error %**	**Blue**	**NIR**	**SWIR**	**TIR**	**MPP %**
Exp.0	0	--	--	--	--	11.2
Exp.1	0	0.0614	0.1867	0.1231	244.858	15.3
Exp.2	5	0.0616	0.1904	0.1278	246.129	16.5
Exp.3	10	0.0617	0.1945	0.1321	247.36	18.4
Exp.4	15	0.0619	0.1971	0.1356	248.407	20.2
Exp.5	20	0.0622	0.2005	0.14	249.518	23.0
Exp.6	25	0.0623	0.2032	0.1426	250.427	25.5
Exp.7	30	0.0622	0.2052	0.145	251.214	27.5
Exp.8	35	0.0626	0.2074	0.1478	252.2	30.0
Exp.9	40	0.0626	0.2092	0.1499	252.902	32.0
Exp.10	45	0.0626	0.2115	0.1524	253.634	34.5
Exp.11	50	0.0628	0.2129	0.1543	254.416	36.4

Fig. 14 illustrates the impact of invalid pixel identification and varying error rates in QA on the performance of the fine-resolution image gap-filling technique (section III.B.2). According to this figure, as the QA error increases, fewer, better-quality pixels are retained to estimate the regressions and

serve as predictors to fill the gaps. Therefore, in each experiment the accuracy of gap-filling is increased. For example, in Exp. 0, where invalid pixel identification was not applied, the R^2 and SSIM values were the lowest, at approximately 50 % and 70 %. Additionally, the error metrics were the highest in this experiment, with MAE and RMSE values of about 0.035 and 0.065. In Exp. 1, the application of the invalid pixel identification technique led to a significant improvement in performance metrics. Specifically, the R^2 value increased to 80%, and the SSIM improved to 88%. Additionally, the MAE and RMSE decreased to 0.01 and 0.028, respectively. These results confirm a notable enhancement in gap-filling accuracy. From Exp. 2 to Exp. 11, as the QA error rate increased, all performance metrics remained approximately comparable with those in Exp. 1, showing no visible changes. This consistency suggests that the technique maintains robust performance despite increasing QA error.

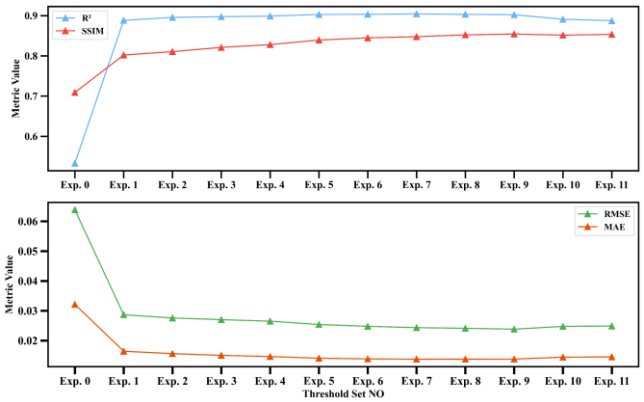

Fig. 14. Sensitivity of fine-resolution image gap-filling to threshold setting. The top plot presents the R^2 and SSIM metrics, comparing reconstructed reflectance values with actual values across experiments, while the bottom plot displays error metrics (RMSE and MAE) for the same experiments. For further details on the experimental setup, see **Table V** and section III.C.2.

V. Discussion

In this study, we introduced an adaptive technique for gap-filling multi-resolution satellite images. This method was applied to gap-filling MODIS and Landsat images and evaluated through a thoughtfully designed set of experiments. The selected test area exhibits distinct characteristics, including undetected clouds (as shown in Fig. 1) which present challenges to gap-filling methods [23], [35], [70]. The discussion of our results is organized in separate subsections addressing different aspects of the study.

A. Key benefits of the gap-identification method

The identification of invalid pixels has a significant impact on gap-filling performance, as shown in section IV.A.1 and IV.B .1 and Fig. 7. According to Fig. 14, when the method relies solely on QA flags for fine-resolution images, the presence of undetected invalid pixels leads to a substantial decrease in gap-filling accuracy. For instance, when the QA layer failed to identify 50% of the invalid pixels (section III.C.2), the RMSE between actual and reconstructed values increased to approximately 0.065. This decline in performance aligns with findings by Wang, et al. [23], who demonstrated similar reductions in gap-filling accuracy under conditions with thin clouds (referred to as invalid pixels in our study). Likewise, the presence of invalid pixels adversely affects the correlation and structural similarity between the gap-filled and original images, as reflected in the SSIM and R^2 metrics (see Fig. 14, Exp. 0). These results highlight the critical role of accurate identification of invalid pixels in ensuring the quality of reconstructed images. Our invalid pixel identification method offers three key benefits: (1) simplicity of implementation, (2) full automation without the need for visual inspection, and (3) rapid execution due to its reliance on a straightforward thresholding method. This approach minimizes computational complexity by avoiding resource-intensive mathematical operations, inherently leading to faster processing times. The use of predefined thresholds, a common approach in detecting clouds, shadows, and other anomalies (often appearing as darker or brighter spots) in satellite images, has been widely documented [71], [83]. However, these methods typically rely on either fixed thresholds or thresholds that require manual adjustment on a day-by-day basis through visual inspection [23], which makes it challenging to automate the process of setting thresholds and identifying invalid pixels. In contrast, our method used the QA flags to automate the threshold-setting process, enabling the detection of any undetected invalid pixels (Fig. 11 (b)). Setting thresholds based on QA flags, which inherently contain some level of error (as illustrated in Fig. 3), requires careful consideration. Our experiments show that errors in the QA led to different threshold settings (Table V). This implies that the number of pixels labeled as invalid by our method increases with higher error rates in the QA layer. While not all of these identified pixels were truly invalid, our gap-filling technique consistently reconstructed them accurately (Fig. 14 Exp .1-11). It may seem unreasonable, but moving from Exp. 1 (MPP = 15.3%) to Exp. 11 (MPP = 36.4%), the estimated regressions applied to fill the gaps remained notably similar. This consistency in the regression estimations explains the stable gap-filling performance, which persisted even as QA error rates increased from 5% to 50%. A selection of these regressions is presented in Table IV. The key advantage of this approach is its ability to maximize the prevention of invalid pixels, ensuring robust and reliable reconstruction.

TABLE IV

Regression details applied to fill the gaps (as described in Section III.B.2) for identified invalid pixels across Experiments 1 to 11. Five invalid pixels were randomly selected as examples to illustrate the results. The reference values correspond to pixel locations in the selected clear image, as explained in the experiment in Section III.C.2. For further details about the experiment, refer to Table V and Section III.C.2.

i	j	Exp	Slope	Intercept	R^2	Predicted	Reference value
187	234	1	0.879824	0.031216	0.895746	0.211598	0.2125
		2	0.879634	0.031262	0.893403	0.211604	
		3	0.878619	0.031504	0.889379	0.211638	
		4	0.876663	0.031903	0.884281	0.211637	
		5	0.869723	0.033773	0.873659	0.212084	
		6	0.854281	0.037659	0.859788	0.212804	
		7	0.848503	0.039289	0.856803	0.213249	
		8	0.836038	0.042009	0.852742	0.213414	
		9	0.880084	0.026816	0.924779	0.22216	
		10	0.845888	0.034938	0.92371	0.222691	
		11	0.846607	0.035292	0.926948	0.223205	
227	41	1	0.888442	0.022738	0.826708	0.188468	0.186293
		2	0.878944	0.025106	0.811678	0.189065	
		3	0.882039	0.024314	0.846535	0.18885	
		4	0.879788	0.024899	0.844005	0.189014	
		5	0.87867	0.025208	0.839814	0.189115	
		6	0.85077	0.032501	0.807167	0.191203	
		7	0.86142	0.029763	0.843667	0.190452	
		8	0.847092	0.03339	0.844492	0.191407	
		9	0.838026	0.035859	0.841512	0.192184	
		10	0.816696	0.041537	0.811542	0.193883	
		11	0.810855	0.043146	0.817792	0.194402	
283	471	1	0.956576	0.015962	0.870611	0.351263	0.25001
		2	0.957932	0.01523	0.871763	0.351006	
		3	0.961213	0.013831	0.870646	0.350758	
		4	0.959378	0.014386	0.870534	0.35067	
		5	0.960696	0.013999	0.873191	0.350745	
		6	0.966014	0.011777	0.873564	0.350387	
		7	0.964778	0.012382	0.874343	0.350559	
		8	0.962318	0.012819	0.875505	0.350133	
		9	0.970878	0.009562	0.877592	0.349876	
		10	0.979775	0.006307	0.880494	0.349741	
		11	0.972328	0.008963	0.88205	0.349786	
6	194	1	0.669237	0.074303	0.740314	0.314996	0.306275
		2	0.668304	0.074652	0.738346	0.315009	
		3	0.668406	0.074629	0.736944	0.315023	
		4	0.666355	0.075316	0.73389	0.314973	
		5	0.662535	0.076671	0.727496	0.314954	
		6	0.662512	0.07695	0.721603	0.315224	
		7	0.66104	0.077627	0.714867	0.315372	
		8	0.660806	0.077656	0.710721	0.315316	
		9	0.663826	0.076972	0.708467	0.315718	
		10	0.662313	0.077625	0.701436	0.315827	
		11	0.668558	0.075271	0.741389	0.315719	
288	330	1	1.37913	-0.07266	0.781555	0.213772	0.21096
		2	1.380058	-0.0729	0.780058	0.213718	
		3	1.381757	-0.07316	0.783825	0.213818	
		4	1.379223	-0.07263	0.78485	0.213817	
		5	1.384476	-0.0739	0.784644	0.213643	
		6	1.38258	-0.07347	0.778575	0.213676	
		7	1.384308	-0.07377	0.776157	0.213733	
		8	1.386328	-0.07423	0.7682	0.21369	
		9	1.385538	-0.07427	0.762023	0.213492	
		10	0.960317	0.005655	0.918927	0.208376	
		11	0.958381	0.006122	0.915951	0.208434	

B. Key benefits of the gap-filling method

In addition to the novel approach for gap identification, our study emphasizes the importance of considering the inherent differences between fine- and coarse-resolution images, as these data types exhibit distinct characteristics [84]. For gap-filling in coarse-resolution images, the method used in this study has also been comprehensively evaluated in our ongoing research, which is currently under review. Moreover, in this work, we demonstrated its capability to reconstruct coarse-resolution reflectance images (Fig. 7). The method was evaluated using artificially introduced random gaps across four spectral bands (Fig. 8), highlighting its outstanding performance, in terms of accuracy of estimated pixel values and structural similarity, when comparing reconstructed and original pixel values across the full range in the fractional abundance of gaps (10% to 90%). This success is attributed to the use of temporal information in creating a reference year (section III.A.2) and an adaptive method that leverages spatial information, ensuring robust performance even when dealing with significant spatial gaps. Gap-filling in fine-resolution images, on the other hand, is more complex due to their lower temporal resolution [85]. The effectiveness of our innovative method for reconstructing invalid pixels in fine-resolution images has been demonstrated in multiple experiments, showing that the impact of gap abundance, size and position is relatively limited. The reconstruction of randomly distributed gaps is easier, since they provide sufficient valid observations within small search windows (section III.B.2, step 1), where the spatial correlation between pixels in the vicinity of gaps is stronger than for those farther away [86]. Consequently, the method performance for random gaps decreased only slightly across gap fractional abundance ranging from 10% to 60% (Fig. 12) for all four spectral bands. This consistency is a key advantage of our gap-filling method in scenarios with distributed gaps. For instance, it can effectively reconstruct stripes caused by the Landsat 7 scan line failure [57], [58], a well-known example of distributed gaps. In contrast, gaps located at the center or corners of an image pose more significant challenges for gap-filling methods. However, when faced with these types of gaps, our method demonstrated strong performance in both scenarios, as highlighted in Table IV. Despite this, a general comparison between the two types of gaps reveals that corner gaps, particularly those with larger sizes, present greater challenges for gap-filling. This is because the method relies on building regression equations using valid observations surrounding the gap. In the case of corner gaps, valid observations are only available on one side of the gap, making it more difficult to meet the minimum correlation threshold (section III.B.2, step 3). In contrast, central gaps benefit from valid observations on all four sides, allowing for the development of stronger regression equations to accurately fill the gaps (Table IV). Overall, our gap-filling method showed exceptional performance when dealing with both types of gaps. The average RMSE for reconstructed pixels compared to original pixels across all gap sizes (10% to 90%) was 0.03 for center gaps and 0.06 for corner gaps. However, a notable difference was observed in the R^2 values: 0.80 for center gaps and 0.68 for corner gaps, highlighting the superior performance of the method in handling center gaps.

C. Method selection and its advantages

The selection of the most appropriate gap-filling method for each specific case was based on a thorough evaluation of the spatial and temporal characteristics of the datasets to ensure optimal performance for both fine- and coarse-resolution data. High-spatial-resolution data present a significant challenge in preserving fine-scale spatial detail, as traditional interpolation methods often introduce distortions or blurring effects [87]. To address this, we employed an adaptive window approach with variable shapes combined with spectral and temporal regression, effectively preserving spatial detail without introducing distortions or blurring artifacts (Fig. 11). In

contrast, for coarse-resolution data, maintaining temporal coherence is critical, as abrupt inconsistencies can lead to misinterpretations in time-series analyses [88]. The selected method for coarse-resolution data successfully preserved temporal continuity while maintaining spatial consistency. Our previous work [67] further supports this finding, demonstrating that the applied approach effectively balances these two key aspects. Thus, our methodology prioritizes spatial consistency for fine-resolution data and temporal stability for coarse-resolution data, ensuring that the reconstructed information aligns with the intrinsic properties of each dataset. The effectiveness of this approach is further supported by the smooth variation in performance across different gap sizes (Fig. 8 and Fig. 12). For coarse-resolution images (see Sect. III.A.2), different gap-filling strategies were employed depending on the gap percentage. The absence of performance jitter (Fig.8) suggests that the applied methods do not introduce abrupt transitions or distortions that could arise from method-induced artifacts. Similarly, for fine-resolution images (see Sect. III.B.2), the adaptive gap-filling approach ensured that regression models are adjusted to local spatial characteristics, with variable-sized search windows maintaining spatial consistency (Fig.12). The smooth variation of performance metrics with gap percentage (Fig. 12) confirms the effectiveness of this strategy, as no artificial discontinuities or anomalies were introduced.

In conclusion, our results suggest that using different gap-filling methods for fine- and coarse-resolution images is advantageous compared to a one-size-fits-all approach. process.

D. Prospective towards data fusion

The methods presented in this study for gap-filling in both fine- and coarse-resolution images offer promising insights for advancing data fusion. Fusion methods, which integrate data from multiple sensors or combine images with different spatial and temporal resolutions (e.g., fine- and coarse-resolution), are instrumental for applications that require continuous and complete datasets [18]. The effectiveness of our gap-filling method in accurately reconstructing pixels across different spectral bands and gap configurations (random, central, and corner) highlights its potential as a foundational component in data fusion. A key strength of our method lies in its ability to manage the complexities of both fine- and coarse-resolution images. The automated invalid pixel identification process for fine images streamlines the detection of clouds, shadows, and other anomalies, eliminating the need for manual intervention. This adaptability is particularly valuable for data fusion, where inconsistencies in data stemming from undetected invalid pixels can compromise the quality of the final output. By incorporating our method's robust pixel identification, fusion methods can effectively minimize the risk of introducing erroneous pixels, thereby enhancing both accuracy and structural integrity in fused images.

Furthermore, the method strong performance in dealing with challenging gap scenarios, such as those located at image corners or centers, demonstrates its potential to improve the resilience of data fusion in addressing variable spatial discontinuities. This capability ensures reliable reconstruction even in complex cases, reinforcing the applicability of our approach in diverse data fusion contexts. The high consistency in performance across gap sizes, particularly for distributed random gaps, where structural similarity and correlation metrics remained robust (Figs. 7 and 11), suggests that our approach could enhance fusion methods that require frequent updates of valid observations. Additionally, the method ability to reconstruct complex patterns in fine-resolution images, including those affected by scan line corrector failures, opens new opportunities for its integration into real-world fusion applications [17].

In summary, our gap-filling technique provides a reliable, automated, and high-performance solution that aligns well with the demands of data fusion methods. The method adaptability, ability to handle diverse gap scenarios, and strong reconstruction performance suggest significant potential for improving the accuracy and usability of data fusion in various applications. Future research could further explore integration strategies for this technique towards improved data fusion and evaluate its effectiveness across different environmental and operational conditions.

E. Method limitations

While our method demonstrates very good performance in gap-filling both fine- and coarse-resolution images, certain limitations must be acknowledged. First, as the gap size increases, the method requires multiple iterations to identify the optimal regression equation for each invalid pixel. This iterative process can significantly impact processing speed, particularly when applied to large images (e.g., exceeding 1000 × 1000 pixels). The computational efficiency of the method is highly dependent on system configuration. On mid-range or standard systems, the gap-filling process is slower, potentially limiting its applicability to large datasets or time-sensitive operations. Additionally, memory usage scales with both the number of missing pixels and the complexity of spatial patterns within the image, requiring high-performance computing resources for optimal execution.

For coarse-resolution images, the computational load remains relatively low due to predefined regression models and the global/local selection approach. However, fine-resolution images require an adaptive search process, where the dynamic selection of neighbouring pixels and regression models increases the computational load. This is particularly pronounced in heterogeneous landscapes, where the method must repeatedly adapt to local variability.

Despite these computational challenges, our approach balances accuracy and efficiency by adaptively selecting regression strategies based on the spatial pattern and fractional cloud cover. Future work may focus on optimizing the algorithm using parallel computing techniques to improve processing speed for large-area applications. Second, the method faces challenges in reconstructing abrupt changes in surface reflectance. Such changes may not be captured in the valid observations surrounding the gap or in data from other dates. In these cases, the performance of gap-filling decreases, as the method relies heavily on spatial and temporal correlations to predict missing values. This limitation is particularly apparent in scenarios involving sudden environmental changes, such as floods or wildfire scars, where the available contextual

data may fail to reflect the true values of many pixels accurately.

To address this, future enhancements of the method could incorporate additional data sources, such as higher temporal resolution imagery, auxiliary environmental datasets (e.g., SAR data for flood detection). Moreover, optimizing computational efficiency remains critical for large-scale applications, and future improvements may include parallel processing techniques or GPU acceleration to reduce processing time while maintaining accuracy.

IV. Conclusion

This study introduces an adaptive system combining different algorithms for gap-filling in both fine- and coarse-resolution satellite images, addressing critical challenges in invalid pixel identification and reconstruction. By leveraging automated threshold-setting processes and spatial temporal correlations, the method effectively detects and reconstructs invalid pixels, even in challenging conditions such as undetected clouds and shadows. The specific combination of algorithms is orchestrated to adapt to each image, mainly on the basis of the fractional abundance and spatial pattern of cloud cover. The approach was rigorously evaluated through a series of experiments involving artificially introduced gaps of varying sizes and positions, demonstrating reliable performance across multiple spectral bands. For fine-resolution imagery, the method consistently achieved good results, particularly for randomly distributed gaps. The RMSE values for the blue band ranged from 0.005 to 0.03, representing the lowest errors, while the NIR band exhibited the highest errors, with RMSE values between 0.01 and 0.05 for gap abundance ranging from 10% to 90%. A similar trend was observed in structural similarity, where SSIM values for the blue band ranged from 0.90 to 0.83, while the red and NIR bands showed values of 0.86 to 0.71, respectively in response to the same changes in gap abundance. Even in more challenging scenarios, such as gaps located at image corners or centers, the method demonstrated adaptability and resilience. For instance, the average RMSE for corner gaps was 0.015, while for center gaps, it was slightly higher at 0.017. SSIM values further highlighted this distinction, with center gaps achieving an average SSIM of 0.80, compared to 0.63 for corner gaps. These results underscore the method ability to maintain high accuracy and structural integrity across diverse gap configurations. For coarse-resolution imagery, the use of temporal information to create a reference year and the adaptive use of spatial data ensured strong reconstruction performance, even for large gaps. Despite its strengths, the method has certain limitations. Computational efficiency is highly dependent on system configuration, particularly for large-scale areas requiring multiple iterations to find optimal regression equations. Additionally, abrupt changes in surface reflectance within a single pixel pose challenges, as these changes may not be adequately captured by valid observations surrounding a gap pixel. Overall, the proposed method provides a reliable and efficient solution for gap-filling, with significant potential benefit to applications that require valid observations, such as the STF method. Additionally, the method holds promise for a wide range of applications, including environmental monitoring, agricultural analysis, and urban planning. Future research could focus on enhancing computational efficiency and addressing scenarios involving abrupt reflectance changes to further expand the method applicability and improve its performance.

Acknowledgment:

The authors would like to thank the reviewers and editors for their valuable comments.

References

[1] V. C. Radeloff *et al.*, "Need and vision for global coarse-resolution Landsat and Sentinel-2 data products", *Remote Sensing of Environment*, vol. 300, p. 113918, 2024/01/01/ 2024, doi: https://doi.org/10.1016/j.rse.2023.113918.

[2] H. Guo *et al.*, "Research on global change scientific satellites," *Science China Earth Sciences*, vol. 57, no. 2, pp. 204-215, 2014/02/01 2014, doi: 10.1007/s11430-013-4748-5.

[3] M. Sigopi, C. Shoko, and T. Dube, "Advancements in remote sensing technologies for accurate monitoring and management of surface water resources in Africa: an overview, limitations, and future directions," *Geocarto International*, vol. 39, no. 1, p. 2347935, 2024/01/01 2024, doi: 10.1080/10106049.2024.2347935.

[4] Z. Tang *et al.*, "Contributions of climate change and urbanization to urban flood hazard changes in China's 293 major cities since 1980," *Journal of Environmental Management*, vol. 353, p. 120113, 2024/02/27/ 2024, doi: https://doi.org/10.1016/j.jenvman.2024.120113.

[5] J. Zhou, L. Jia, M. v. Hoek, M. Menenti, J. Lu, and G. Hu, "An optimization of parameter settings in HANTS for global NDVI time series reconstruction," in *2016 IEEE International Geoscience and Remote Sensing Symposium (IGARSS)*, 10-15 July 2016 2016, pp. 3422-3425, doi: 10.1109/IGARSS.2016.7729884.

[6] B. Wu *et al.*, "Challenges and opportunities in remote sensing-based crop monitoring: A review," *National Science Review*, vol. 10, no. 4, p. nwac290, 2023.

[7] Z. Yi, L. Jia, and Q. Chen, "Crop Classification Using Multi-Temporal Sentinel-2 Data in the Shiyang River Basin of China," *Remote Sensing*, vol. 12, no. 24, p. 4052, 2020. [Online]. Available: https://www.mdpi.com/2072-4292/12/24/4052.

[8] P. Li, L. Jia, J. Lu, M. Jiang, C. Zheng, and M. Menenti, "Investigating the Response of Vegetation to Flash Droughts by Using Cross-Spectral Analysis and an Evapotranspiration-Based Drought Index," *Remote Sensing*, vol. 16, no. 9, p. 1564, 2024.

[9] M. Menenti *et al.*, "Analysis of vegetation response to climate variability using extended time series of multispectral satellite images," *Remote sensing optical observations of vegetation properties*, vol. 131, p. 164, 2010.

[10] Q. Chen *et al.*, "A data-driven high spatial resolution model of biomass accumulation and crop yield: Application to a fragmented desert-oasis agroecosystem," *Ecological Modelling*, vol. 475, p. 110182, 2023/01/01/ 2023, doi: https://doi.org/10.1016/j.ecolmodel.2022.110182.

[11] [11] Z. Yi, L. Jia, Q. Chen, M. Jiang, D. Zhou, and Y. Zeng, "Early-Season Crop Identification in the Shiyang River Basin Using a Deep Learning Algorithm and Time-Series Sentinel-2 Data," *Remote Sensing*, vol. 14, no. 21, p. 5625, 2022. [Online]. Available: https://www.mdpi.com/2072-4292/14/21/5625.

[12] M. Menenti *et al.*, "Multi-Source Hydrological Data Products to Monitor High Asian River Basins and Regional Water Security," *Remote Sensing*, vol. 13, no. 24, p. 5122, 2021. [Online]. Available: https://www.mdpi.com/2072-4292/13/24/5122.

[13] C. Zheng *et al.*, "Integrating hydrologic modeling and satellite remote sensing to assess the performance of sprinkler irrigation," *Geo-spatial Information Science*, vol. 27, no. 3, pp. 934-952, 2024/05/03 2024, doi: 10.1080/10095020.2024.2344615.

[14] C. Zheng, L. Jia, and G. Hu, "Global land surface evapotranspiration monitoring by ETMonitor model driven by multi-source satellite earth observations," *Journal of Hydrology*, vol. 613, p. 128444, 2022/10/01/ 2022, doi: https://doi.org/10.1016/j.jhydrol.2022.128444.

[15] H. R. Ghafarian, M. Menenti, L. Jia, and H. den Ouden, "Reconstruction of cloud-free time series satellite observations of land surface temperature," *EARSel eProc*, vol. 11, pp. 123-131, 2012.

[16] J. Yang *et al.*, "A Robust Method for Generating High-Spatiotemporal-Resolution Surface Reflectance by Fusing MODIS and Landsat Data," *Remote Sensing*, vol. 12, no. 14, p. 2312, 2020. [Online]. Available: https://www.mdpi.com/2072-4292/12/14/2312.

[17] Y. Luo, K. Guan, and J. Peng, "STAIR: A generic and fully-automated method to fuse multiple sources of optical satellite data to generate a high-resolution, daily and cloud-/gap-free surface reflectance product," *Remote Sensing of Environment*, vol. 214, pp. 87-99, 2018/09/01/ 2018, doi: https://doi.org/10.1016/j.rse.2018.04.042.

[18] J. Xiao, A. K. Aggarwal, N. H. Duc, A. Arya, U. K. Rage, and R. Avtar, "A review of remote sensing image spatiotemporal fusion: Challenges, applications and recent trends," *Remote Sensing Applications: Society and Environment*, vol. 32, p. 101005, 2023/11/01/ 2023, doi: https://doi.org/10.1016/j.rsase.2023.101005.

[19] D. Guo, W. Shi, M. Hao, and X. Zhu, "FSDAF 2.0: Improving the performance of retrieving land cover changes and preserving spatial details," *Remote Sensing of Environment*, vol. 248, p. 111973, 2020/10/01/ 2020, doi: https://doi.org/10.1016/j.rse.2020.111973.

[20] Y. Ma *et al.*, "STEPSBI: Quick spatiotemporal fusion with coarse- and fine-resolution scale transformation errors and pixel-based synthesis base image pair," *ISPRS Journal of Photogrammetry and Remote Sensing*, vol. 206, pp. 1-15, 2023/12/01/ 2023, doi: https://doi.org/10.1016/j.isprsjprs.2023.10.016.

[21] H. Liu *et al.*, "Reconstruction of seamless harmonized Landsat Sentinel-2 (HLS) time series via self-supervised learning," *Remote Sensing of Environment*, vol. 308, p. 114191, 2024/07/01/ 2024, doi: https://doi.org/10.1016/j.rse.2024.114191.

[22] Q. Wang, Y. Tang, X. Tong, and P. M. Atkinson, "Filling gaps in cloudy Landsat LST product by spatial-temporal fusion of multi-scale data," *Remote Sensing of Environment*, vol. 306, p. 114142, 2024/05/15/ 2024, doi: https://doi.org/10.1016/j.rse.2024.114142.

[23] Q. Wang, L. Wang, X. Zhu, Y. Ge, X. Tong, and P. M. Atkinson, "Remote sensing image gap filling based on spatial-spectral random forests," *Science of Remote Sensing*, vol. 5, p. 100048, 2022/06/01/ 2022, doi: https://doi.org/10.1016/j.srs.2022.100048.

[24] Q. Cheng, H. Shen, L. Zhang, Q. Yuan, and C. Zeng, "Cloud removal for remotely sensed images by similar pixel replacement guided with a spatio-temporal MRF model," *ISPRS Journal of Photogrammetry and Remote Sensing*, vol. 92, pp. 54-68, 2014/06/01/ 2014, doi: https://doi.org/10.1016/j.isprsjprs.2014.02.015.

[25] I. Tsardanidis, A. Koukos, V. Sitokonstantinou, T. Drivas, and C. Kontoes, "Cloud gap-filling with deep learning for improved grassland monitoring," *arXiv preprint arXiv:2403.09554*, 2024.

[26] Z. Tang, "Gap-filling using machine learning: implementations and applications in remote sensing," University of Helsinki, Finland, 2022.

[27] C. Guillemot and O. L. Meur, "Image Inpainting : Overview and Recent Advances," *IEEE Signal Processing Magazine*, vol. 31, no. 1, pp. 127-144, 2014, doi: 10.1109/MSP.2013.2273004.

[28] A. C. Siravenha, D. Sousa, A. Bispo, and E. Pelaes, "Evaluating Inpainting Methods to the Satellite Images Clouds and Shadows Removing," in *Signal Processing, Image Processing and Pattern Recognition*, Berlin, Heidelberg, T.-h. Kim, H. Adeli, C. Ramos, and B.-H. Kang, Eds., 2011// 2011: Springer Berlin Heidelberg, pp. 56-65.

[29] C. Yu, L. Chen, L. Su, M. Fan, and S. Li, "Kriging interpolation method and its application in retrieval of MODIS aerosol optical depth," in *2011 19th International Conference on Geoinformatics*, 24-26 June 2011 2011, pp. 1-6, doi: 10.1109/GeoInformatics.2011.5981052.

[30] N. Siabi, S. H. Sanaeinejad, and B. Ghahraman, "Effective method for filling gaps in time series of environmental remote sensing data: An example on evapotranspiration and land surface temperature images," *Computers and Electronics in Agriculture*, vol. 193, p. 106619, 2022/02/01/ 2022, doi: https://doi.org/10.1016/j.compag.2021.106619.

[31] M. Menenti, S. Azzali, W. Verhoef, and R. van Swol, "Mapping agroecological zones and time lag in vegetation growth by means of fourier analysis of time series of NDVI images," *Advances in Space Research*, vol. 13, no. 5, pp. 233-237, 1993/05/01/ 1993, doi: https://doi.org/10.1016/0273-1177(93)90550-U.

[32] W. Verhoef, "Application of harmonic analysis of NDVI time series (HANTS)," *Fourier analysis of temporal NDVI in the Southern African and American continents*, vol. 108, pp. 19-24, 1996.

[33] G. Roerink, M. Menenti, and W. Verhoef, "Reconstructing cloudfree NDVI composites using Fourier analysis of time series," *International journal of remote sensing*, vol. 21, no. 9, pp. 1911-1917, 2000.

[34] J. Zhou, L. Jia, and M. Menenti, "Reconstruction of global MODIS NDVI time series: Performance of Harmonic ANalysis of Time Series (HANTS)," *Remote Sensing of Environment*, vol. 163, pp. 217-228, 2015/06/15/ 2015, doi: https://doi.org/10.1016/j.rse.2015.03.018.

[35] D. J. Weiss, P. M. Atkinson, S. Bhatt, B. Mappin, S. I. Hay, and P. W. Gething, "An effective approach for gap-filling continental scale remotely sensed time-series," (in eng), *ISPRS J Photogramm Remote Sens*, vol. 98, pp. 106-118, Dec 2014, doi: 10.1016/j.isprsjprs.2014.10.001.

[36] K. Liu, X. Li, S. Wang, and H. Zhang, "A robust gap-filling approach for European Space Agency Climate Change Initiative (ESA CCI) soil moisture integrating satellite observations, model-driven knowledge, and spatiotemporal machine learning," *Hydrol. Earth Syst. Sci.*, vol. 27, no. 2, pp. 577-598, 2023, doi: 10.5194/hess-27-577-2023.

[37] Z. Tang, G. Amatulli, P. K. E. Pellikka, and J. Heiskanen, "Spectral Temporal Information for Missing Data Reconstruction (STIMDR) of Landsat Reflectance Time Series," *Remote Sensing*, vol. 14, no. 1, p. 172, 2022. [Online]. Available: https://www.mdpi.com/2072-4292/14/1/172.

[38] Q. Zhou, G. Xian, and H. Shi, "Gap Fill of Land Surface Temperature and Reflectance Products in Landsat Analysis Ready Data," *Remote Sensing*, vol. 12, no. 7, p. 1192, 2020. [Online]. Available: https://www.mdpi.com/2072-4292/12/7/1192.

[39] Q. Wang, Y. Tang, Y. Ge, H. Xie, X. Tong, and P. M. Atkinson, "A comprehensive review of spatial-temporal-spectral information reconstruction techniques," *Science of Remote Sensing*, vol. 8, p. 100102, 2023/12/01/ 2023, doi: https://doi.org/10.1016/j.srs.2023.100102.

[40] X. Zhang *et al.*, "GLC_FCS30D: the first global 30 m land-cover dynamics monitoring product with a fine classification system for the period from 1985 to 2022 generated using dense-time-series Landsat imagery and the continuous change-detection method," *Earth System Science Data*, vol. 16, no. 3, pp. 1353-1381, 2024.

[41] J. Zhou *et al.*, "Sensitivity of six typical spatiotemporal fusion methods to different influential factors: A comparative study for a normalized difference vegetation index time series reconstruction," *Remote Sensing of Environment*, vol. 252, p. 112130, 2021/01/01/ 2021, doi: https://doi.org/10.1016/j.rse.2020.112130.

[42] Y. Wang, X. Zhou, Z. Ao, K. Xiao, C. Yan, and Q. Xin, "Gap-Filling and Missing Information Recovery for Time Series of MODIS Data Using Deep Learning-Based Methods," *Remote Sensing*, vol. 14, no. 19, p. 4692, 2022. [Online]. Available: https://www.mdpi.com/2072-4292/14/19/4692.

[43] N.-W. Park and P. C. Kyriakidis, "A Geostatistical Approach to Spatial Quality Assessment of Coarse Spatial Resolution Remote Sensing Products," *Journal of Sensors*, vol. 2019, no. 1, p. 1, 2019, doi: https://doi.org/10.1155/2019/7297593.

[44] S. Kandasamy, F. Baret, A. Verger, P. Neveux, and M. Weiss, "A comparison of methods for smoothing and gap filling time series of remote sensing observations–application to MODIS LAI products," *Biogeosciences*, vol. 10, no. 6, pp. 4055-4071, 2013.

[45] H. R. Ghafarian Malamiri *et al.*, "Comparison of harmonic analysis of time series (HANTS) and multi-singular spectrum analysis (M-SSA) in reconstruction of long-gap missing data in NDVI time series," *Remote Sensing*, vol. 12, no. 17, p. 2747, 2020.

[46] J. Pascual-Granado, R. Garrido, and J. Suárez, "MIARMA: A minimal-loss information method for filling gaps in time series-Application to CoRoT light curves," *Astronomy & Astrophysics*, vol. 575, p. A78, 2015.

[47] C. Huang, Q. Zhuang, X. Meng, P. Zhu, J. Han, and L. Huang, "A fine spatial resolution modeling of urban carbon emissions: a case study of Shanghai, China," *Scientific Reports*, vol. 12, no. 1, p. 9255, 2022.

[48] R. P. Sishodia, R. L. Ray, and S. K. Singh, "Applications of Remote Sensing in Precision Agriculture: A Review," *Remote Sensing*, vol. 12, no. 19, p. 3136, 2020. [Online]. Available: https://www.mdpi.com/2072-4292/12/19/3136.

[49] S. R. Schill *et al.*, "Regional High-Resolution Benthic Habitat Data from Planet Dove Imagery for Conservation Decision-Making and Marine Planning," *Remote Sensing*, vol. 13, no. 21, p. 4215, 2021. [Online]. Available: https://www.mdpi.com/2072-4292/13/21/4215.

[50] G. Z. Xian *et al.*, "Improving temporal frequency of Landsat surface temperature products using the gap-filling algorithm," US Geological Survey, 2331-1258, 2023.

[51] X. Li *et al.*, "Assessing the effects of time interpolation of NDVI composites on phenology trend estimation," *Remote Sensing*, vol. 13, no. 24, p. 5018, 2021.

[52] R. Zhang *et al.*, "Detecting the spatiotemporal variation of vegetation phenology in northeastern China based on MODIS NDVI and solar-induced chlorophyll fluorescence dataset," *Sustainability*, vol. 15, no. 7, p. 6012, 2023.

[53] N. Zeng, X. Ren, H. He, L. Zhang, P. Li, and Z. Niu, "Estimating the grassland aboveground biomass in the Three-River Headwater Region of China using machine learning and Bayesian model averaging," *Environmental Research Letters*, vol. 16, no. 11, p. 114020, 2021.

[54] J. Chen, X. Zhu, J. E. Vogelmann, F. Gao, and S. Jin, "A simple and effective method for filling gaps in Landsat ETM+ SLC-off images," *Remote Sensing of Environment*, vol. 115, no. 4, pp. 1053-1064, 2011/04/15/ 2011, doi: https://doi.org/10.1016/j.rse.2010.12.010.

[55] G. Yin, G. Mariethoz, Y. Sun, and M. F. McCabe, "A comparison of gap-filling approaches for Landsat-7 satellite data," *International Journal of Remote Sensing*, vol. 38, no. 23, pp. 6653-6679, 2017.

[56] G. Yin, G. Mariethoz, and M. F. McCabe, "Gap-filling of landsat 7 imagery using the direct sampling method," *Remote Sensing*, vol. 9, no. 1, p. 12, 2016.

[57] Y. Li, Q. Liu, S. Chen, and X. Zhang, "An Improved Gap-Filling Method for Reconstructing Dense Time-Series Images from LANDSAT 7 SLC-Off Data," *Remote Sensing*, vol. 16, no. 12, p. 2064, 2024.

[58] C. Zeng, H. Shen, and L. Zhang, "Recovering missing pixels for Landsat ETM+ SLC-off imagery using multi-temporal regression analysis and a regularization method," *Remote Sensing of Environment*, vol. 131, pp. 182-194, 2013.

[59] Y. Chen et al., "Cloud and Cloud Shadow Detection Based on Multiscale 3D-CNN for High Resolution Multispectral Imagery," *IEEE Access*, vol. 8, pp. 16505-16516, 2020, doi: 10.1109/ACCESS.2020.2967590.

[60] H. Han, C. Han, T. Lan, L. Huang, C. Hu, and X. Xue, "Automatic Shadow Detection for Multispectral Satellite Remote Sensing Images in Invariant Color Spaces," *Applied Sciences*, vol. 10, no. 18, p. 6467, 2020 https://www.mdpi.com/2076-3417/10/18/6467.

[61] Y. Zhang, L. Ji, X. Xu, P. Zhang, K. Jiang, and H. Tang, "A Flexible Spatiotemporal Thick Cloud Removal Method with Low Requirements for Reference Images," *Remote Sensing*, vol. 15, no. 17, p. 4306, 2023. https://www.mdpi.com/2072-4292/15/17/4306.

[62] Y. Lei, X. Gao, Y. Kou, B. Wu, Y. Zhang, and B. Liu, "Balanced Cloud Shadow Compensation Method in High-Resolution Image Combined with Multi-Level Information," *Applied Sciences*, vol. 13, no. 16, p. 9296, 2023. https://www.mdpi.com/2076-3417/13/16/9296.

[63] A. M. Wilson, B. Parmentier, and W. Jetz, "Systematic land cover bias in Collection 5 MODIS cloud mask and derived products — A global overview," *Remote Sensing of Environment*, vol. 141, pp. 149-154, 2014/02/05/ 2014, doi: https://doi.org/10.1016/j.rse.2013.10.025.

[64] T. Shen-Chuan, C. Peng-Yu, and C. Chian-Yen, "Missing pixels restoration for remote sensing images using adaptive search window and linear regression," *Journal of Electronic Imaging*, vol. 25, no. 4, p. 043017, 8/1 2016, doi: 10.1117/1.JEI.25.4.043017.

[65] H. Guo, Y. Zheng, H. Xu, and L. Bruzzone, "Clear: A Novel Gap-Filling Method for Optical Remote Sensing Images Combining Class-Based Linear Regression and Iterative Residual Compensation," *Available at SSRN 4884873*, 2024.

[66] C. B. Schaaf *et al.*, "First operational BRDF, albedo nadir reflectance products from MODIS," *Remote sensing of Environment*, vol. 83, no. 1-2, pp. 135-148, 2002.

[67] S. Afsharipour, L. Jia, and M. Menenti, "A New Flexible Approach for Reconstructing Satellite-Based Land Surface Temperature Images: A Case Study With MODIS Data", *IEEE Journal of Selected Topics in Applied Earth Observations and Remote Sensing*, 2025, pp. 1-18 (pre-access). doi: 10.1109/JSTARS.2025.3545404.

[68] S. Shiff, D. Helman, and I. M. Lensky, "Worldwide continuous gap-filled MODIS land surface temperature dataset," *Scientific Data*, vol. 8, no. 1, p. 74, 2021/03/04 2021, doi: 10.1038/s41597-021-00861-7.

[69] M. Ahmed, R. Seraj, and S. M. S. Islam, "The k-means Algorithm: A Comprehensive Survey and Performance Evaluation," *Electronics*, vol. 9, no. 8, p. 1295, 2020. [Online]. Available: https://www.mdpi.com/2079-9292/9/8/1295.

[70] L. Sun, X. Liu, Y. Yang, T. Chen, Q. Wang, and X. Zhou, "A cloud shadow detection method combined with cloud height iteration and spectral analysis for Landsat 8 OLI data," *ISPRS Journal of Photogrammetry and Remote Sensing*, vol. 138, pp. 193-207, 2018/04/01/ 2018, doi: https://doi.org/10.1016/j.isprsjprs.2018.02.016.

[71] K. Liang *et al.*, "A Novel Method for Cloud and Cloud Shadow Detection Based on the Maximum and Minimum Values of Sentinel-2 Time Series Images," *Remote Sensing*, vol. 16, no. 8, p. 1392, 2024. [Online]. Available: https://www.mdpi.com/2072-4292/16/8/1392.

[72] K. Ge, J. Liu, F. Wang, B. Chen, and Y. Hu, "A Cloud Detection Method Based on Spectral and Gradient Features for SDGSAT-1 Multispectral Images," *Remote Sensing*, vol. 15, no. 1, p. 24, 2023. [Online]. Available: https://www.mdpi.com/2072-4292/15/1/24.

[73] E. Özelkan, "Water body detection analysis using NDWI indices derived from landsat-8 OLI," *Polish Journal of Environmental Studies*, vol. 29, no. 2, pp. 1759-1769, 2020.

[74] G. S. Santecchia, G. N. Revollo Sarmiento, S. A. Genchi, A. J. Vitale, and C. A. Delrieux, "Assessment of Landsat-8 and Sentinel-2 Water Indices: A Case Study in the Southwest of the Buenos Aires Province (Argentina)," (in eng), *J Imaging*, vol. 9, no. 9, Sep 18 2023, doi: 10.3390/jimaging9090186.

[75] [71] B.-C. Gao, "NDWI—A normalized difference water index for remote sensing of vegetation liquid water from space," *Remote sensing of environment*, vol. 58, no. 3, pp. 257-266, 1996.

[76] R. Kour, N. Patel, and A. P. Krishna, "Assessment of relationship between snow cover characteristics (SGI and SCI) and snow cover indices (NDSI and S3)," *Earth Science Informatics*, vol. 8, pp. 317-326, 2015.

[77] A. Kulkarni, J. Srinivasulu, S. Manjul, and M. P, "Field based spectral reflectance studies to develop NDSI method for snow cover monitoring," *Journal of the Indian Society of Remote Sensing*, vol. 30, pp. 73-80, 2002.

[78] W. Tobler, "On the first law of geography: A reply," *Annals of the association of American geographers*, vol. 94, no. 2, pp. 304-310, 2004.

[79] R. L. Lagendijk, P. M. B. van Roosmalen, J. Biemond, A. Rareș, and M. J. T. Reinders, "3.11 - Video Enhancement and Restoration," in *Handbook of Image and Video Processing (Second Edition)*, A. L. Bovik Ed. Burlington: Academic Press, 2005, pp. 275-VI.

[80] G. Chen *et al.*, "Spatiotemporal fusion for spectral remote sensing: A statistical analysis and review," *Journal of King Saud University - Computer and Information Sciences*, vol. 35, no. 3, pp. 259-273, 2023/03/01/ 2023, doi: https://doi.org/10.1016/j.jksuci.2023.02.021.

[81] B. Marchant, S. Platnick, K. Meyer, and G. Wind, "Evaluation of the MODIS Collection 6 multilayer cloud detection algorithm through comparisons with CloudSat Cloud Profiling Radar and CALIPSO CALIOP products," *Atmospheric Measurement Techniques*, vol. 13, no. 6, pp. 3263-3275, 2020.

[82] S. A. Ackerman, R. E. Holz, R. Frey, E. W. Eloranta, B. Maddux, and M. McGill, "Cloud detection with MODIS. Part II: validation," *Journal of Atmospheric and Oceanic Technology*, vol. 25, no. 7, pp. 1073-1086, 2008.

[83] Z. Li, H. Shen, Q. Weng, Y. Zhang, P. Dou, and L. Zhang, "Cloud and cloud shadow detection for optical satellite imagery: Features, algorithms, validation, and prospects," *ISPRS Journal of Photogrammetry and Remote Sensing*, vol. 188, pp. 89-108, 2022/06/01/ 2022, doi: https://doi.org/10.1016/j.isprsjprs.2022.03.020.

[84] L. Yan and D. P. Roy, "Large-Area Gap Filling of Landsat Reflectance Time Series by Spectral-Angle-Mapper Based Spatio-Temporal Similarity (SAMSTS)," *Remote Sensing*, vol. 10, no. 4, p. 609, 2018. [Online]. Available: https://www.mdpi.com/2072-4292/10/4/609.

[85] G. Z. Xian *et al.*, "Improving temporal frequency of Landsat surface temperature products using the gap-filling algorithm," in "Open-File Report," Reston, VA, Report 2023-1006, 2023. [Online]. Available: https://pubs.usgs.gov/publication/ofr20231006

[86] N. Karasiak, J. F. Dejoux, C. Monteil, and D. Sheeren, "Spatial dependence between training and test sets: another pitfall of classification accuracy assessment in remote sensing," *Machine Learning*, vol. 111, no. 7, pp. 2715-2740, 2022/07/01 2022, doi: 10.1007/s10994-021-05972-1.

[87] X. Zhang and X. Wu, "Image interpolation by adaptive 2-D autoregressive modeling and soft-decision estimation," *IEEE transactions on image processing*, vol. 17, no. 6, pp. 887-896, 2008.

[88] Y. Kim, P. C. Kyriakidis, and N.-W. Park, "A cross-resolution, spatiotemporal geostatistical fusion model for combining satellite image time-series of different spatial and temporal resolutions," *Remote Sensing*, vol. 12, no. 10, p. 1553, 2020

Seyedkarim Afsharipour received the M.Sc. degree in remote sensing and GIS from the Faculty of Geography, University of Tehran, Tehran, Iran, in 2018. He is currently pursuing the Ph.D. degree at the State Key Laboratory of Remote Sensing and Digital Earth, Aerospace Information Research Institute, Chinese Academy of Sciences, Beijing, China.

His research interests include earth observation data gap-filling and fusion, multi-sensor data integration, land surface analysis, and energy balance models. He is particularly focused on the development of advanced spatiotemporal fusion techniques to enhance the resolution and continuity of remote sensing observations. His work also involves analyzing surface energy fluxes, land-atmosphere interactions, and the impacts of environmental variability on land surface processes using remote sensing and geospatial modeling approaches.

Li Jia (Member, IEEE) received the B.S. degree in meteorology from the Beijing College of Meteorology, Beijing, China, in 1988, the M.Sc. degree in atmospheric physics from the Chinese Academy of Sciences, Beijing, in 1997, and the Ph.D. degree in environmental science from Wageningen University, Wageningen, The Netherlands, in 2004. She is currently a professor at the State Key Laboratory of Remote Sensing and Digital Earth, Aerospace Information Research Institute, Chinese Academy of Sciences. Her research interests include the Earth observations from ground, airborne and spaceborne and their applications in hydrometeorology, water resource, agriculture and climate change. She developed the ETMonitor model based on satellite remote sensing observations to estimate evapotranspiration and generate multi-scale evapotranspiration products. She is currently a member of the GEWEX-SSG (Global Energy and Water Exchanges Program - Scientific Steering Group), and a member of the GCOS-TOPC.

Massimo Menenti, received the Laurea degree in physics from the Università di Roma, Rome, Italy, in 1972, and the Dr. Sc. degree in environmental sciences from the Delft University of Technology, Delft, Netherlands in 1984. He has held senior research and faculty positions at Wageningen University, at the École Nationale Supérieure des Physique de Strasbourg (ENSPS), France., the National Research Council of Italy and the Delft University of Technology, The Netherlands. He is currently a professor at the Institute of Tibetan Plateau Research, Chinese Academy of Sciences, China, at the State Key Laboratory of Remote Sensing and Digital Earth, Aerospace Information Research Institute, Chinese Academy of Sciences, China and at the Delft University of Technology, The Netherlands.

His research interests include land surface processes, remote sensing of land-atmosphere interactions, surface energy balance modeling, and hydrological cycle analysis. He has made ground-breaking and early contributions to the development of remote sensing methodologies for water resource management, climate change studies, and land surface temperature retrieval. His research integrates multi-source satellite observations with numerical models to improve environmental monitoring and prediction.

Prof. Menenti has served as an editor and reviewer for multiple geoscience and remote sensing journals. He has played a leading role in various international research collaborations, including projects with ESA, NASA, and the European Union, focusing on earth observation, climate change, and hydrological modeling.

Hamid Reza Ghafarian Malamiri received the B.S. degree in Soil and Water Engineering from Tehran University, Tehran, Iran, in 2000, the M.Sc. degree in Geoinformatics from Twente University, Enschede, The Netherlands, in 2007, and the Ph.D. degree in Remote Sensing from Delft University of Technology, Delft, The Netherlands, in 2014. He is currently an Associate Professor at the Department of Remote Sensing at Yazd University, Yazd, Iran. His research interests include Earth observation from ground-, airborne-, and spaceborne platforms and its applications in thermal remote sensing, water resource management, precision agriculture, and urban management. He developed a model to estimate soil thermal properties and soil temperature at different soil depths based on time-series satellite observations.